Czech Technical University in Prague

Faculty of Nuclear Sciences and Physical Engineering

Department of physics

Calibrations of AugerPrime detector upgrade

RESEARCH PROJECT

Author: Margita Majerčáková
Supervisor: RNDr. Martina Boháčová Ph.D.
Year: 2021

ČESKÉ VYSOKÉ UČENÍ TECHNICKÉ

Fakulta Jaderná a Fyzikálně Inženýrská

Katedra fyziky

Kalibrace detektorů AugerPrime

VÝZKUMNÝ ÚKOL

Vypracoval: Margita Majerčáková
Vedoucí práce: RNDr. Martina Boháčová Ph.D.
Rok: 2021

Prohlášení

Prohlašuji, že jsem svou bakalářskou práci vypracovala samostatně a použila jsem pouze podklady (literaturu, projekty, SW atd.) uvedené v přiloženém seznamu.

V Praze dne .....

.....
Margita Majerčáková

Acknowledgment

I would like to express my gratitude to my supervisor, RNDr. Martina Boháčová Ph.D. for her advice, helpful discussions and guidance. I am also thankful to Dr. Eva Maria Martins dos Santos for help with the software and RNDr. Petr Tobiška Ph.D. for his corrections on this work.

Margita Majerčáková

Název práce:
Kalibrace detektorů AugerPrime

Autor: Margita Majerčáková

Druh práce: Výzkumný úkol

Vedoucí práce: RNDr. Martina Boháčová Ph.D.
Fyzikální ústav AV ČR
Konzultant: –

Abstrakt: Kozmické žiarenie najvyšších energí stále ostáva záhadou aj po rokoch vytrvalého skúmania. Otázky týkajúce sa jeho pôvodu, zloženia a mechanizmov, vďaka ktorým je urýchľované na takú vysokú energiu sa očakávajú byť viac zodpovedané upgradeom Observatória Pierra Augera nazývaným AugerPrime. Hlavný cieľ tohto vylepšenia je väčšie rozlíšenie miónovej a elektromagnetickej zložky spŕšky za pomoci inštalácie nového scintilačného detektoru na každú stanicu pôvodných vodných Čerenkovových detektorov. Táto práca je zamerná hlavne na štúdium systematiky a kalibrácie povrchového detektora. Skúmané témy sa venujú dlhodobému vývoju kalibračných jenotiek, opisu novej metódy kalibrácie detektorov za využitia scintilátor a zmenám kalibračných histogramov po pridaní scintilačného detektora. Nakoniec sú uvedené výsledky testovania vybraných vlastnosti novej elektroniky inštalovanej na povrchových detektoroch Observatória.
Klíčová slova: Observatórium Pierra Augera, AugerPrime upgrade, kalibračné histogramy, VEM, UUB

Title:
Calibrations of AugerPrime detector upgrade

Author: Margita Majerčáková

Abstract: Cosmic rays of the highest energies remain mysterious even after years of their observation. The questions concerning their origin, composition and acceleration mechanisms they undergo are expected to be answered with the new upgrade of the Pierre Auger Observatory called AugerPrime. The upgrade main goal is to disentangle the muonic and electromagnetic component of the shower with the help of the added scintillation detector. This work is dedicated to the study of the systematic effects and calibration of the Water Cherenkov detectors together with the Scintillator detectors. The topics studied in this work include the long term evolution of the calibration quantities, a new approach to the calibration of the surface detector stations using the scintillator signal and the changes in the calibration histograms after the addition of the scintillator. Finally, the behavior of chosen properties of the new electronics deployed in the array is tested.
Key words: The Pierre Auger Observatory, AugerPrime upgrade, calibration histograms, VEM, UUB

Contents

Introduction

The discovery of cosmic rays was made more than a century ago. Since then, the properties of these cosmic particles were observed by many scientists. However, each new finding raised a number of new unanswered questions. Energies of the most energetic particles ever observed, that are striking the atmosphere, are of many orders higher than energies at which particles are accelerated in a man-made accelerators. Where do they come from? What are the processes that accelerate them to such high energies?
Unfortunately for the physicists, the most energetic particles have the lowest observed flux and thus the large areas are needed to observe them. The largest astroparticle experiment currently operating is The Pierre Auger Observatory located in Argentina. The Observatory is using hybrid detection method by simultaneous measurement of air shower by ground-based detectors and fluorescence telescopes. The Observatory is presently in the process of implementing new improvements, that should help with answering the important questions. The main aim of this upgrade is to disentangle the muonic and the electromagnetic component of an air shower and thus derive the chemical composition of primary rays. With the knowledge of the composition, the information needed to refute or confirm existing theoretical explanations will be provided.

This document is organized as follows:
In the first chapter of this work, the basic features of cosmic rays are described. The most observed subject, their energy spectrum with leading possible explanations of its features are presented. Possible mechanisms of their acceleration and sources are introduced, and finally the extensive air showers and their components are described.
The next chapter is aimed at the Pierre Auger Observatory. The detection principles and the construction of both main detectors, the fluorescence telescope and also the surface Water Cherenkov Detector are briefly described. The most significant results of the Observatory are presented.
The third chapter is dedicated to the upgrade of the Observatory called the AugerPrime upgrade. In the beginning, the motivation for this upgrade and also the expected goals is presented. The individual parts of the upgrade are described, with focus on the main part, the Scintillator Detector.
A separated chapter is devoted to the explanation of the calibration and data processing of the surface detector stations.
The practical part of this work begins with the prepared calibration histograms of the stations with both old and new versions of electronics. Next section focuses on the long term evolution of the calibration units - VEM and MIP and the study

of the impact of the added scintillator on the calibration histograms of the Water Cherenkov Detectors. In the next part, a new important approach on the calibration of the detectors by using the Scintillator Detector is presented and the final part is dedicated to testing various features of new electronics in the array.

Chapter 1

Cosmic rays

Cosmic rays were discovered by Victor Hess in 1912 [1]. They are high energy charged particles which arrive to the Earth's atmosphere, coming from various sources, such as stars, active galactic nuclei, supernovae explosions of stars and others. They are mostly composed of nuclei of atoms, protons being the most abundant, and then from other particles like electrons, positrons, antiprotons etc, which are thought to be created by interactions of the primary particles with the intergalactic gas.
Some of these are undoubtedly the most energetic particles we can observe in nature since the big bang (up to 10^{20} eV). They may have many orders of magnitude more energy than particles artificially accelerated in big accelerators like the LHC.
These particles are important to observe, because they carry information about processes in the universe.

1.1 Energy spectrum

Energies of the primary particles extend over a broad range from a few MeVs to 10^{20} MeV. The flux of particles we observe is decreasing with increasing energy. Fig. 1.1 shows the energy spectrum of cosmic rays as measured by various experiments. On the vertical axis is the flux of primary cosmic rays. It is scaled by a factor $E^{2.6}$ for better recognition of anomalies. The flux of primary cosmic rays we observe at Earth obeys so called power law, i.e, the flux of particles behaves according to [2]

$$N(E)dE \sim E^{-\gamma}dE, \tag{1.1}$$

where γ is the spectral factor varying through the spectrum close to the value 2.7. This figure possesses three distinctive features. The knee, around 3×10^{15} MeV, where the flux is steepening and $\gamma \sim 3.1$ [3], second knee around 10^{17} eV, where flux is steepening even more with $\gamma \sim 3.3$ and ankle at 4×10^{18} eV, where the spectrum flattens and γ changes again to 2.7.

The origin of these features is still not certain, but the most accepted explanation states, that the decrease of flux near the knee is caused by galactic sources reaching maximum acceleration potential for lighter nuclei (protons). Decrease around

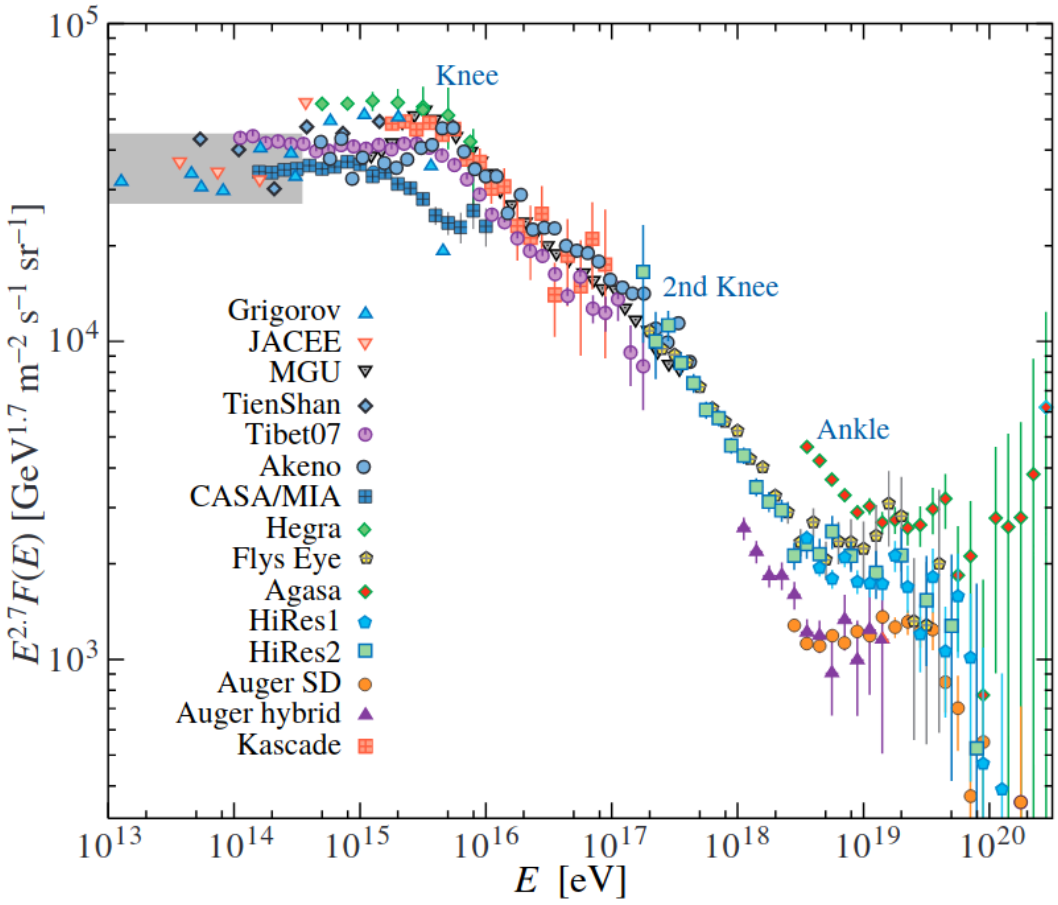

Figure 1.1: Spectrum of cosmic rays, reconstructed from air shower measured by marked experiments. The grey box highlights the region, where cosmic rays were observed directly [4].

second knee is explained similarly for heavier elements. Around the ankle the spectrum slightly increases again. This is probably caused by a change from galactic to extragalactic sources [2]. At the end of the measured spectrum we observe a flux suppression, which is thought to be due to the maximum acceleration potential of extragalactic sources or GZK (more in the Section 1.3).

1.2 Sources and acceleration

The low energy cosmic rays up to few GeV are known to be produced in the Sun, but the source of the most energetic cosmic rays is still unknown. This is mainly attributed to the fact, that these particles arrives at the Earth with very low rates, as can be seen from the flux suppression in 1.1. It is also a mystery, what objects can accelerate particles to such enormous energies.

For cosmic rays, two main production scenarios are being considered: top-down and bottom-up scenarios [1]. The top-down scenario states that high-energy cosmic rays come from a decay of heavy, exotic particles, whereas in the bottom-up scenarios, particles are produced with low energies and then accelerated. However, measured data from astroparticle experiments gathered up to now (upper limits on photon and neutrino fluxes) do not support the top-down scenario [5].

Sources

Even though the sources of high energy particles are still uncertain, a number of possible scenarios has been proposed to explain them. The most convincing way of explanation is based on the radius of a source and its strength of magnetic field. To understand this model, we must fisrtly define the Larmour radius. The Larmor radius of the particle R_L, where [6]

$$R_L = EqB, \tag{1.2}$$

is the radius of a circular trajectory that particle with energy E and charge q will follow in a presence of a uniform magnetic field of strength B. If we impose a geometrical condition on the trajectory, that it must not exceed the size of the accelerator, we obtain a limit on maximum energy a particle can gain:

$$E_{\max} \propto qBL. \tag{1.3}$$

The maximum energy $E_{\max}$ a particle can be accelerated to is thus dependent on its charge q, the magnetic field of the object B and the radius of the region, in which it is accelerated R. This is called the Hillas equation. If a particle escapes from the region where it was being accelerated, it would be unable to gain more energy. The possible sources of cosmic rays plotted according to this critetion are in the Hillas plot in Fig. 1.2.

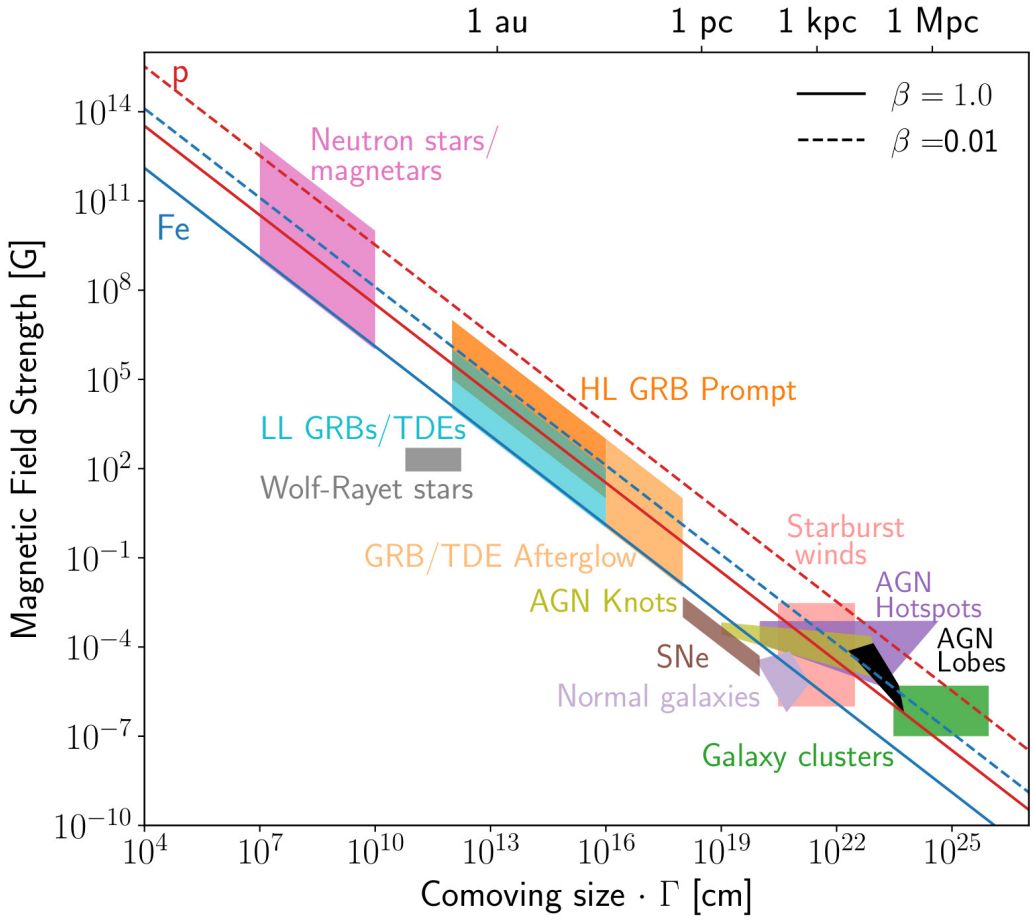

Figure 1.2: Hillas plot. It shows the relation between the strength of magnetic field of source and its size for a maximum energy particle can be accelerated to [7].

Fermi mechanism

In 1949, Enrico Fermi proposed a model on acceleration of charged particles in the supernova remnants called The Fermi Mechanism [8]. Charged cosmic rays can be accelerated by strong turbulent magnetic fields as they can induce variable electric fields an thus accelerate.

This model uses the fact, that after gravitational collapse of a star, shock waves of strong magnetic fields are produced. These are able to accelerate cosmic rays to very high energies.

The first model of acceleration is called "second-order Fermi acceleration mechanism". Cosmic rays entering moving magnetized clouds undergo multiple elastic scattering as depicted in Fig. 1.3 on the right. They are accelerated by a variable magnetic field in a cloud. The energy particles can gain per collision is of order β^2, where β is the relativistic velocity of a cloud. This way of acceleration is not very effective, because for clouds in a galaxy, $\beta \sim 10^{-4}$.

In the other model of acceleration called "first-order Fermi acceleration mechanism", charged particles can gain energy of the order β. The difference in this mechanism is

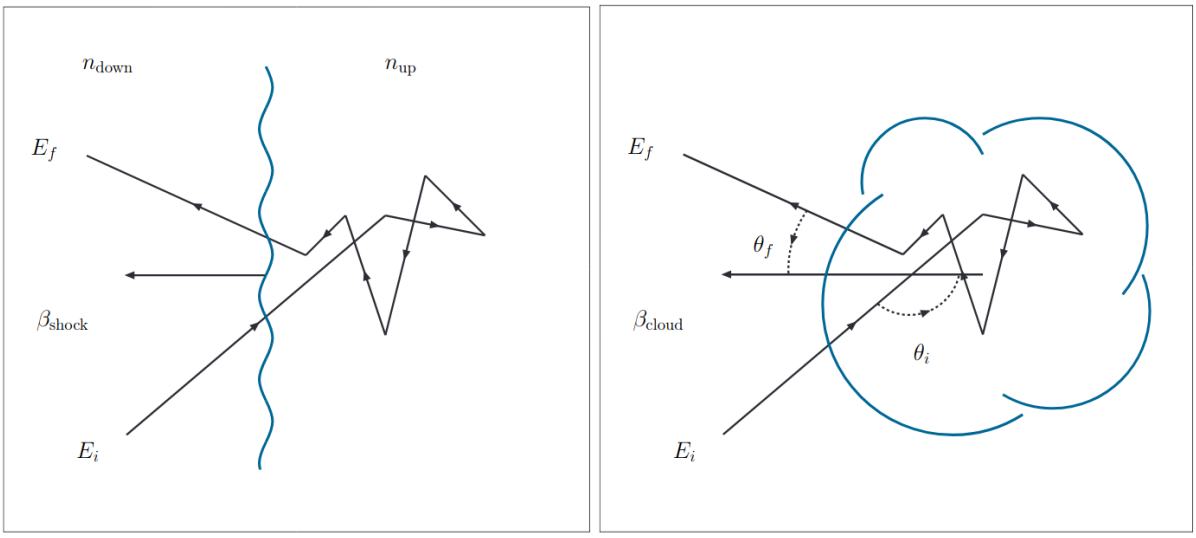

Figure 1.3: Left: The first-order Fermi acceleration. Right: Second order Fermi acceleration [9].

that the charged particles interact with a shock wave front of a magnetized matter and are accelerated by moving between regions inside (downstream) and outside (upstream) the shock front (diffusive shock acceleration) depicted in Fig. 1.3 on the left.

1.3 Propagation

Cosmic rays traveling through the Universe interact not only with magnetic fields that can change their trajectory and travel time but also with other particles that can cause energy losses. The most significant ones are caused by interactions with the cosmic microwave background (CMB).

For the lightest nuclei like protons above the energy of 6×10^{19} eV [10] , the main process is the pion photoproduction through Delta resonance:

$$p + \gamma \rightarrow \Delta^{+} \rightarrow p + \pi^{0} \tag{1.4}$$

$$p + \gamma \rightarrow \Delta^{+} \rightarrow n + \pi^{+} \tag{1.5}$$

In these interactions protons lose about 20% of their energy.
In 1966 Greisen, Zatsepin and Kutzin [11] independently calculated the limit based on these interactions, that sets restrictions on energy of protons from distant sources. This limit is concerning the fact, that over large distances, any protons with energies over the threshold energy will lose majority of their energy. The limit is called by the initials of their names - GZK. The particles above the GZK limit will therefore most probably arrive from sources relatively close to Earth.

Next common process is photodisintegration of nuclei:

$$N + \gamma \rightarrow N + e^{-} + e^{+} \tag{1.6}$$

which is a decay of a nucleus into nucleons after excitation by photons.

Besides the interactions with CMB, cosmic rays can lose energy due to expansion of the Universe.

1.4 Extensive air showers

It is visible from the spectrum of cosmic rays, that the flux is significantly decreasing with increasing energy of incoming particles. This fact disfavors a direct observation of cosmic rays at highest energies.

A better approach is to detect them indirectly at the ground, using the atmosphere as a detection medium. Primary particles passing through the atmosphere interact with molecules of air producing secondary particles. These can generate more and more particles forming a cascade of particles, which is referred to as an extensive air shower as shown in Fig. 1.4. This shower can be measured by ground based particle detectors.

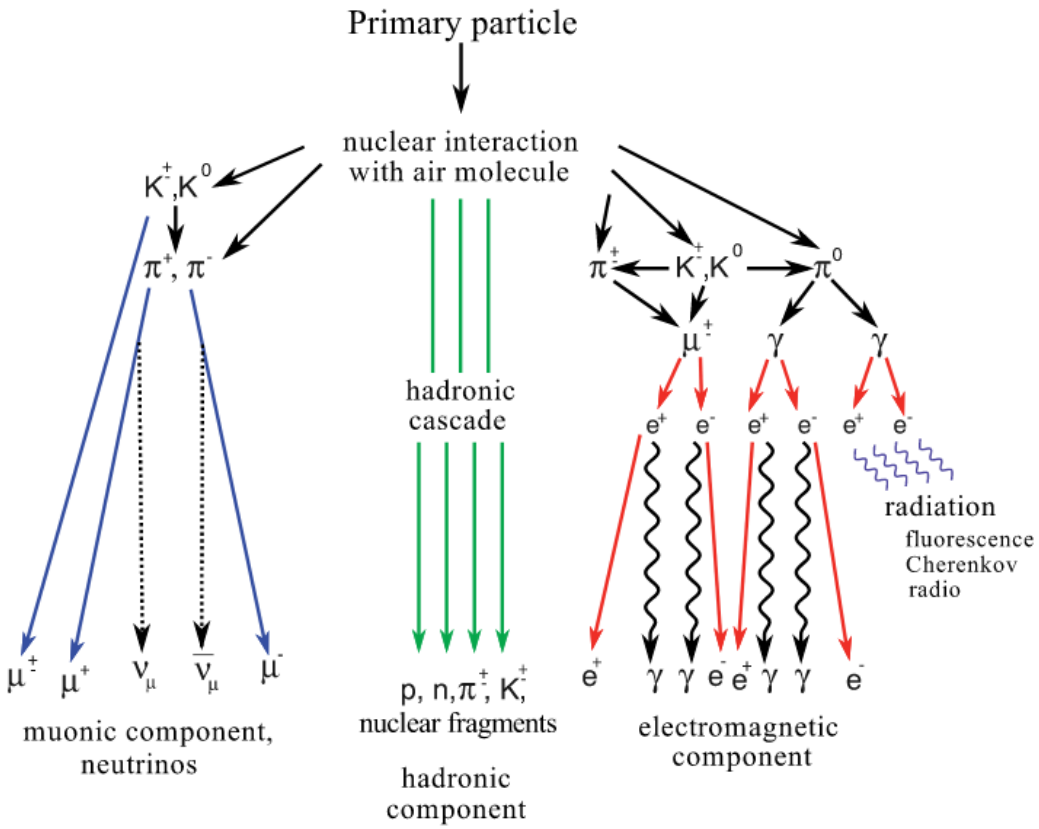

Figure 1.4: Representation of an extensive air shower induced by a primary cosmic ray [14].

Particles contained in an air shower can be divided into three different components: hadronic, electromagnetic and muonic [12],[13].

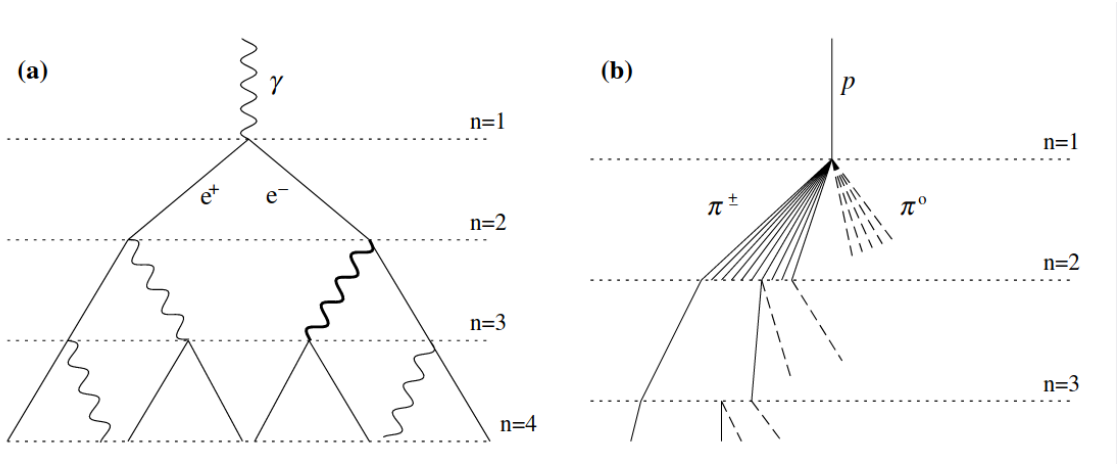

Figure 1.5: (a) Heitler model for electromagnetic cascades. (b) Modified Heitler-Matthews model for hadronic cascades [12].

Hadronic component

Hadronic component consists of protons neutrons and particles that are produced by hadronic interactions with air nucleus, mainly pions and kaons. This component is created mostly in the beginning of the shower, carrying almost 75% of the total energy and quickly decays. Fig. 1.5 shows the modified Heitler-Matthews model for hadronic cascades.

When a hadron collides with air nucleus, all charged and uncharged pions are created approximately in equal parts. Neutral pions immediately decay into two photons:

$$\pi^0 \rightarrow \gamma + \gamma, \tag{1.7}$$

which contribute to the electromagnetic component.

Charged pions can further interact and produce more mesons until their energies drop to critical value E_c^π ($E_c^\pi \approx 20$GeV in air [12]). After the pions reach the E_c^π they decay to muons producing also neutrinos:

$$\pi^- \rightarrow \mu^- + \bar{\nu}_\mu, \tag{1.8}$$

$$\pi^+ \rightarrow \mu^+ + \nu_\mu. \tag{1.9}$$

The total energy of neutrinos is not easily detectable and so it contributes to the so-called invisible energy. It accounts for $\sim 5\%$ of the total energy.

Muonic component

Muonic component consists of muons produced in the decay of the charged mesons, $\pi^\pm$, $K^\pm$. These muons extend to the ground. The number of μ in a shower can be approximated as:

$$N_\mu = \left(\frac{E_0}{E_c}\right)^\alpha \quad \alpha = \ln\frac{n_{ch}}{n_{tot}}, \tag{1.10}$$

where n_{ch} is number of charged particles in a shower and n_{tot} number of all particles in a shower.

We can further derive the relationship of the number of muons in a shower to mass composition of primary cosmic ray by following superposition principle.

If the shower was created by heavy nuclei with mass A and energy E, it can be approximated as A number of nucleons with energy E/A. Considering this, we can express the number of muons in a shower as

$$N_\mu = A\left(\frac{E_0/A}{E_c}\right)^\alpha = A^{1-\alpha}\left(\frac{E_0}{E_c}\right)^\alpha \tag{1.11}$$

Therefore, the heavier the primary, the more muons are produced.

The electromagnetic component

The electromagnetic component of an air shower consists of electrons, positrons and photons. It can be described by simple Heitler model shown in Fig. 1.5, that was later improved with other interactions. However, the simple model illustrates the important interactions well.

It accounts for two contributing processes. A photon interacts with air nucleus creating positron and electron pair,

$$\gamma \to e^+ + e^-. \tag{1.12}$$

Electron then interacts with the Coulomb field of nucleus producing bremsstralung photon

$$e^- \to e^- + \gamma. \tag{1.13}$$

The number of particles starts decreasing, when photons or electrons reach the critical energy $E_c = 85\mathrm{MeV}$ [12], at which the energy loss by ionization is equal to the radiative energy loss.

A shower contains the most particles right before the moment, when the number of particles starts to decrease. This moment is described by a measured observable X_{max}, the depth at which the shower reach its maximum development.

About 90% of the total energy of a shower at the ground is in the electromagnetic component.

Chapter 2

The Pierre Auger Observatory

The Pierre Auger Observatory is presently the largest running astroparticle experiment [15]. It is located in Argentina, Mendoza province and it is spread over large area of 3000 km^2 because it was proposed to observe and examine cosmic rays with energies above 10^{17} eV, where the flux of the particles is very low. The location was chosen for various factors. The main reason was the convenience of building an observatory in the southern hemisphere, as it would observe the centre of our galaxy. Good weather conditions and low light pollution also contributed to the decision, and finally, the altitude across the array is roughly the same and suitable for the measurement of the maximum of a shower development for high-energy particles. The Observatory uses a hybrid method of detection of cosmic rays. This means, that two types of detectors are used, the SD (surface detector) and the FD (fluorescence detector), which work on different principles but together they can (under special conditions) provide better and more accurate measurements.

2.1 Surface detector array

The surface detector array consists of more than 1660 Water Cherenkov detectors (WCDs) spaced in a grid spread over the area of around 3000 km^2. In the main array, the stations are 1500 m apart (SD-1500) and the positioning is fully efficient in the detection of a primary particle with energy over 3×10^{18} eV. The main array was also filled by smaller arrays with the 750 m spacing and 433 m spacing, both used for lower energies.

The stations of surface detector array are made of plastic tanks with a radius of 1.8 m filled with 12 000 l of purified water up to height of 1.2 m contained in a special diffusive, highly-reflective liner. Three photo-multipliers (PMTs) are installed at the top of the tank watching the water volume. They are equipped with a positive voltage divider, the photocathodes being grounded due to their closeness to water. PMTs collect Cherenkov photons produced by particles passing the water faster than the speed of light in water. The signal from PMT is read out from the anode and from the last dynode and digitized with flash analog to digital converters (10 bit, 40 MHz). Signal from the last dynode is multiplied by a factor of 32, providing a

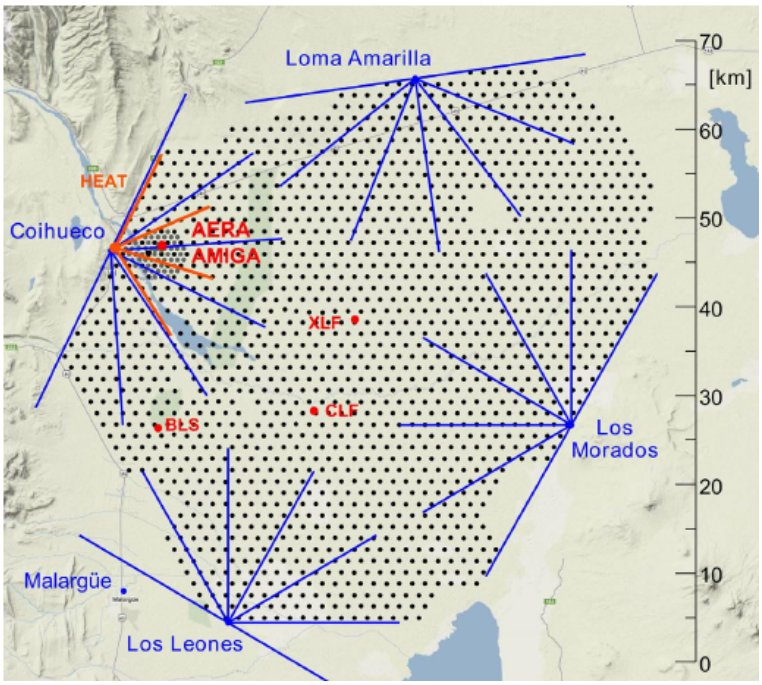

Figure 2.1: The map of SD array of the Pierre Auger Observatory with marked sites with fluorescence detectors [15].

higher dynamic range. In case the shower core is close to the station, the signal from the dynode can be saturated, but signal from anode can still be used. For showers more distant to the station the amplified signal from the last dynode will be more distinguishable from background. The maximum signal that can be recorded and not saturated corresponds to the signal from a 100 EeV cosmic ray distant about 500 m from the shower core [15].

Each station is also equipped with a GPS reciever and an antenna for timing and data transmission.

2.2 Fluorescence detector array

The fluorescence detector array is made up by 24 fluorescence telescopes located on four different sites, Los Leones, Los Morados, Loma Amarilla and Coihueco. These telescopes look at $30° \times 30°$ in azimuth and elevation. Each site consist of a building with six telescopes, so that it covers 180° in azimuth. Such a site and the setup of a telescope is shown in Fig. 2.3.

When a charged particle produced in a shower passes the atmosphere, it can excite atmospheric nitrogen. De-excitation of nitrogen is accompanied by emission of light in the UV part of spectrum (300-430 nm). Wavelengths of the fluorescence light overlap the visible light spectrum (which begins at $\sim$ 380 nm), thus the detector can operate only during dark, moonless nights. The detector is also sensitive to the weather and due to these circumstances its duty cycle is only 13%.

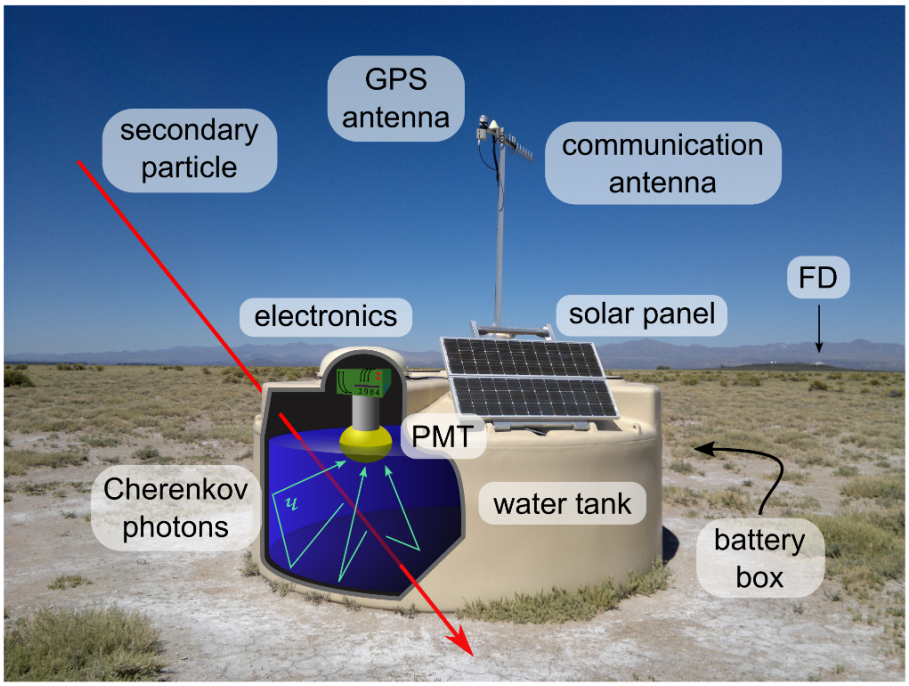

Figure 2.2: Surface detector station of the Pierre Auger Observatory [13].

The telescopes are composed of UV-passing filter, correction optics and a segmented mirror, that focuses the light onto a camera formed by photomultipliers. Whereas the fluorescence light is proportional to the energy deposited in the atmosphere, it can be obtained by integrating the longitudinal development profile of a shower $\frac{dE}{dX}(X)$, where X is atmospheric slant depth.

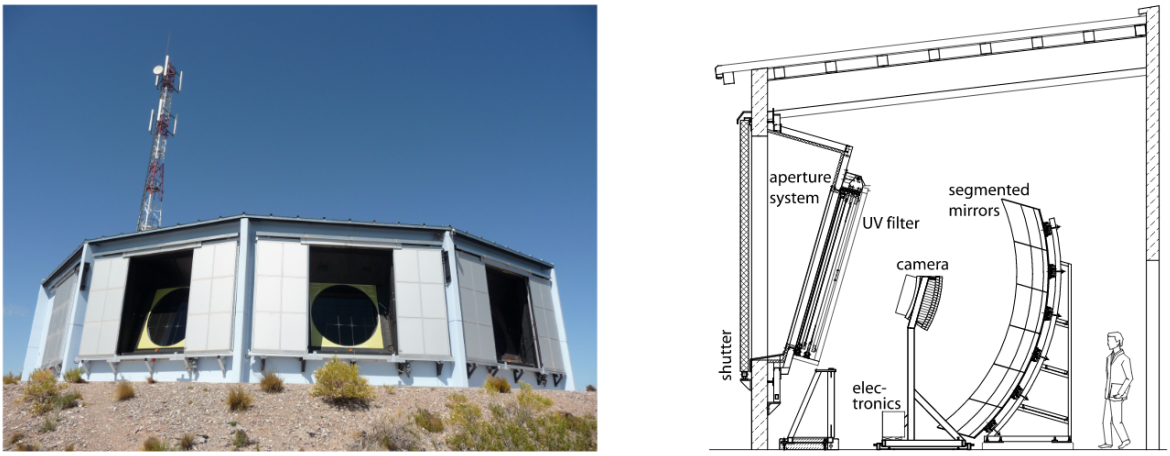

Figure 2.3: The site of FD array and described parts of telescope [15].

2.3 Enhancements of the Observatory

Apart from the main detectors FD and SD, the Observatory was gradually enhanced with different detectors and upgrades.

AMIGA

The Auger Muon and Infilled Ground Array - AMIGA, started operating in 2015 comprises two parts. First is a lower energy extension to the SD and second focuses on the muonic component of the shower. The latter is still in the process of deployment.

The area of 23.5 km^2 was filled with additional WCDs, creating SD infill array with spacing 750 m (SD-750) that is fully efficient at lower energies (above 3×10^{17} eV) compared to the main array. The muon detectors were installed in the infill array, buried at a depth of 2.3 m near the WCDs. The soil shields the detectors and thus ensures, that only muons will be detected. The muon detectors are composed of 4 plastic scintillators, two with the area of 10 m^2 each and two smaller with the area of 5 m^2. [22]. The layout of the detectors can be seen in Fig. 2.4.

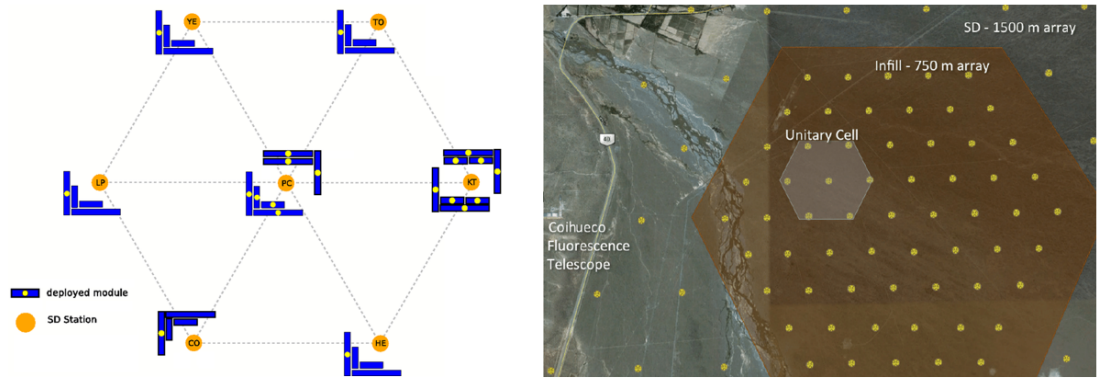

Figure 2.4: Left: Layout of the AMIGA Unitary Cell. Yellow dots are SD stations and blue rectangles are muon detectors. Right: Map of the Infill array with marked unitary cell [23].

HEAT

In addition to the 24 fluorescence telescopes, 3 HEAT - High Elevation Auger Telescopes have been deployed to the array. These telescopes can be tilted and thus look at different angles, from 30° to 60° in elevation. They are implemented near the Coihueco site and overlook the SD-750 to observe showers initialized by particles with lower energies (above 10^{17}), as these particles have the maximum of their shower development higher in the atmosphere [24].

AERA

The Auger Engineering Radio Array - AERA, is composed of 153 radio antennas covering the area of 17 km^2 in SD-750, completed in 2015. The antennas measure the radio emission of the electromagnetic component of the shower in the frequency range of 30 MHz to 80 MHz. The energy threshold for primary particles is approximately 10^{17} eV. Two different types of antennas are used, logarithmic periodic dipole antennas and butterfly antennas (see Fig. 2.5) with almost 100% duty cycle [25].

Figure 2.5: Antennas used in the Observatory for the detection of the electromagnetic component of a shower. Left: A logarithmic periodic dipole antenna. Right: A butterfly antenna [25].

2.4 Selected results of the Pierre Auger Observatory

The Pierre Auger Observatory, being the largest astroparticle experiment, running for more than 20 years, has published many experimental findings in physics of ultra-high energy.

The Observatory has firmly supported the flux suppression in the energy spectrum above 4×10^{19} eV [26] visible in Fig. 2.6.

Other interesting results have been achieved in the chemical composition of cosmic rays. The type of primary particle affects the depth of the shower maximum. Fig 2.7 shows measured distributions of X_{max} in small energy bins. The red and blue lines, representing distributions of X_{max} for proton and iron, are derived from hadronic interaction models. These results indicate the dominance of lighter nuclei up to around $10^{18.3}$ eV. For even higher energies, the X_{max} tends to heavier components [29].

The number of muons in a shower has also been in the interest of the Observatory, because it is also an observable sensitive to the mass composition. The results from the Observatory are shown in Fig. 2.8, where the large discrepancy between models

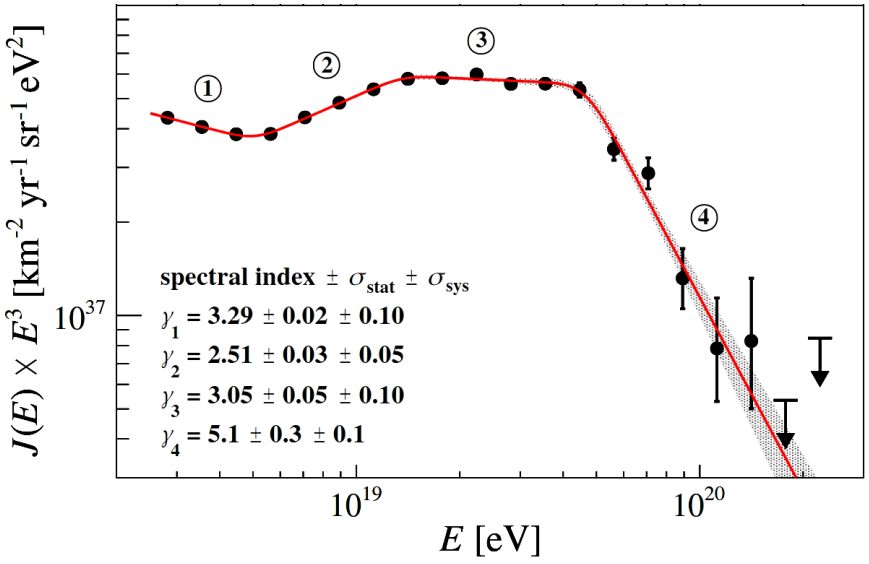

Figure 2.6: The measured energy spectrum of cosmic rays with visible flux suppresion. The grey area marks the uncertainty. [27].

and data is noticable. This discovery supports the conclusion that the hadronic interaction models are not complete and particles above the LHC energies may behave and interact differently then we think [28].

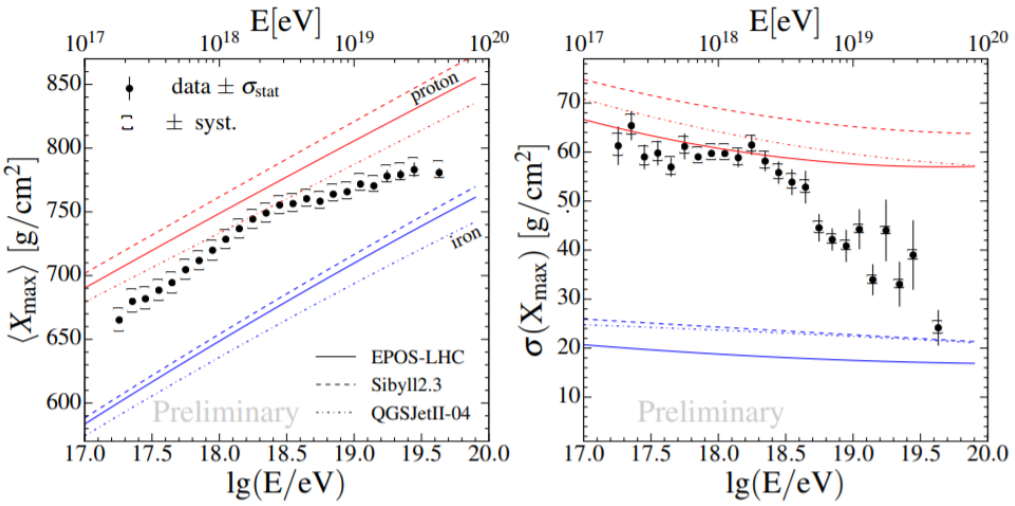

Figure 2.7: The measured data of $\langle X_{\max} \rangle$ and $X_{\max}$ standard deviation for different energies of the primary particle. The red and blue lines represent distributions of $X_{\max}$ for proton and iron that are derived from hadronic interaction models [29].

The next impressive conclusion has been achieved in the question of origin of cosmic rays. If they originated in our galaxy, the direction of the maximum flux would be pointing to the galactic center. The Observatory found a significant dipolar anisotropy for energies above 8×10^{18} eV. The flux is approximately 6.5% above average in one certain direction, that is 120° away from the galactic center. This can

be seen in Fig. 2.9. The result thus strongly supports assumption, that cosmic rays of such high energy are of extragalactic origin [30].

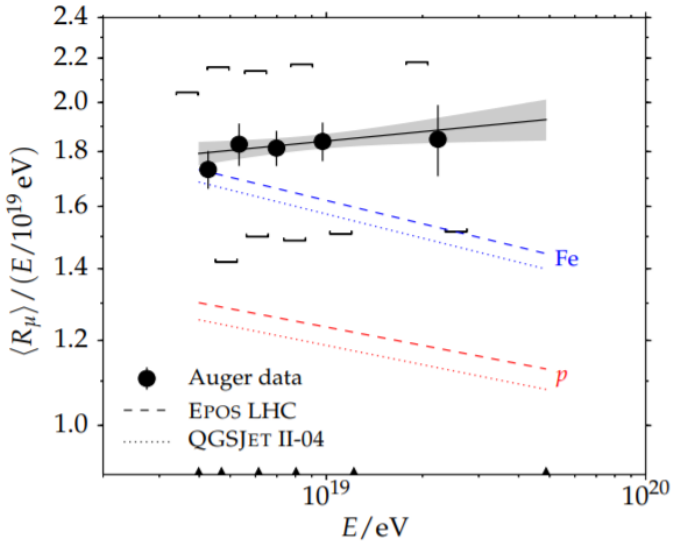

Figure 2.8: Average content of muons $\langle R_\mu \rangle$ per shower energy E as a function of energy E. The red and blue lines represent values for proton and iron derived from hadronic interaction models [28].

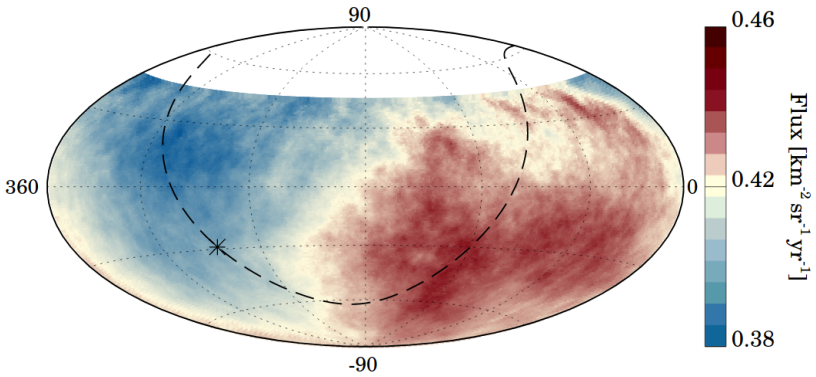

Figure 2.9: Map of fluxes of particles with energy above 8×10^{18} eV in galactic coordinates. The Galactic plane is represented with a dashed line and the Galactic center is marked with a star. [30].

The Observatory has also studied proton-proton and proton-air cross sections [31] and further set the limits on neutrino [33] and photon [32] searches at the highest energies.

Chapter 3

AugerPrime upgrade

Some results measured by the Observatory were discussed in the previous chapter. Nevertheless, some findings arise even more questions than answers in physics of ultra-high energy cosmic rays. The presence of knees, ankle and a suppresion in the spectrum, the origin and acceleration of cosmic rays and even hadronic interactions at such energies are not convincingly explained. Determining a mass composition of the primary cosmic ray would significantly help to answer these questions.

The decision of upgrading SD stations comes from the fact, that low duty cycle of FD in combination with low flux of particles at the highest energies, results in indecisive statistics to make certain conclusions about mass composition of primary cosmic rays.

AugerPrime is the upgrade of the Pierre Auger Observatory currently under deployment [34]. The main part of this upgrade is placing thin scintillators on top of each water Cherenkov detector. This improvement aims at observing both the electromagnetic and the muonic component of the shower, where the relative signals of the scintillation and water-Cherenkov detectors allow for disentangling these shower components on event by event basis. A small photomultiplier tube is also being added to each water-Cherenkov station in order to increase the dynamic range of the SD. The upgrade also includes muon detectors buried under the SD stations in a small region of the Observatory and lastly the electronics is being upgraded with a new unified SD readout board, on which all functionalities required by the old and new detectors are jointly implemented.

3.1 Motivation and goals of the AugerPrime upgrade

3.1.1 Mass composition

Mass composition of the primary cosmic ray is of the outermost importnace to propose neutrino and gamma ray flux limits and further understand the acceleration

potential of sources of cosmic rays, losses due to propagation and their origins.

The composition can be studied by measuring mass composition sensitive observables such as the depth of the shower maximum $X_{\max}$ and number of muons at $X_{\max}$, $N^{\mu}_{\max}$.

The depth of the maximum shower development

The $X_{\max}$ distributions for different energies, measured by the fluorescence telescopes of the Pierre Auger Observatory, were used to estimate the mass composition of cosmic rays. Four mass groups were fitted to the distributions with three different models of hadronic interactions (EPOSLHC, QGSJet and Sibyll). The results can be seen in Fig. 3.1.

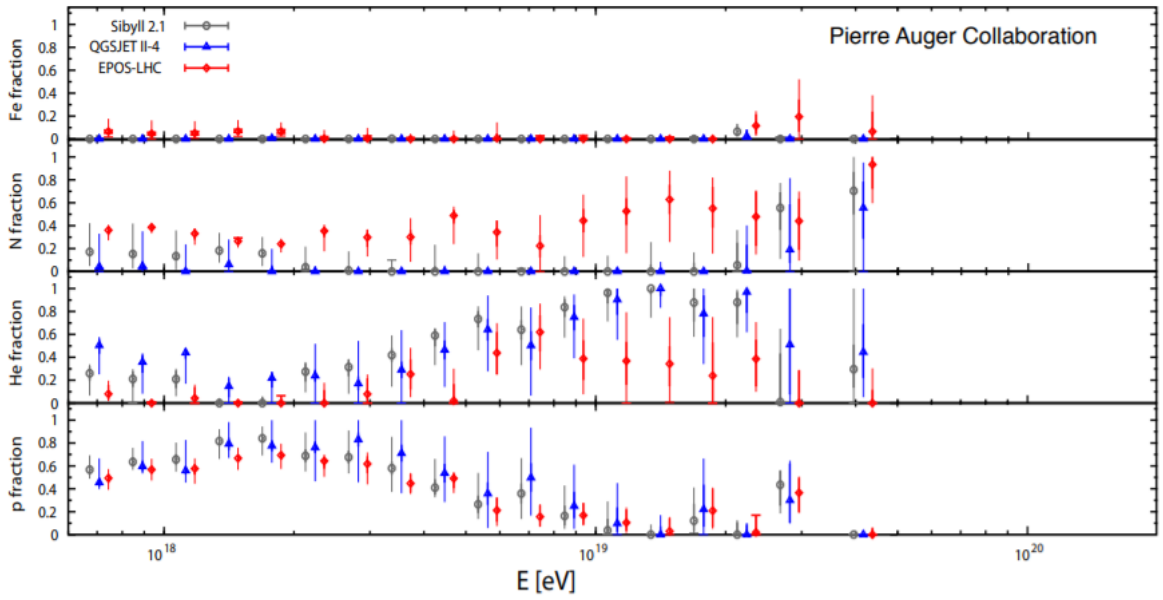

Figure 3.1: Estimation of the mass composition of ultra-high energy cosmic rays. The Xmax distributions measured by the FD have been fitted by a superposition of four mass groups [35].

If one pays attention to the development of a proton fraction, it can be noticed, that this fraction becomes large in the vicinity of the ankle. Another observation is the change from lighter to heavier components. Around 10^{19} eV, the helium component increases with proton component decreasing and it is suggested, that similarly the change from helium to nitrogen appears at higher energy, however, the statistics of the data are not conclusive. Lastly, we can observe the indications of re-appearance of a proton component at the highest energies. These protons are of severe importance because they are not deflected by galactic magnetic fields as heavier nuclei and therefore are supposed to point out to their sources.

These results were explained with different astrophysical scenarios. Some of them are explained here. Further information is available in [34].

Maximum rigidity scenario In this scenario, it is considered, that sources can accelerate particles up to the energy corresponding to their charge (maximum rigidity). The heavier the particle, the more it will be accelerated, therefore, in the end of the spectrum there should ocur r heavier particles almost exclusively. The flux suppression is described then as a consequence of sources reaching their maximum acceleration potential.

Photo-disintegration scenario In this case it is suspected, that heavier nuclei are photo-disintegrated on cosmic microwave background photons and therefore the lighter elements corresponds to fragments of these disintegrated nuclei. The flux suppression is then instinctively a consequence of energy loss processes (photo-disintegration). It is also supposed that almost no light elements are accelerated in the sources.

Proton-dominance model As it is apparent from the name of this model, it assumes that the flux observed is made up mostly of extragalactic protons at energies above 10^{18} eV. The flux suppression is related to pion-photoproduction. This model also brings explanation to the existence of the ankle as a result of e^+e^- pair production.

The muonic component

The X_{max} is directly observable only with the FD detector with low duty cycle, therefore it is more convenient to also measure a different mass sensitive observable with 100% duty cycle of SD. Strong candidate is the number of muons in a shower, N^{μ}_{max}, if it is possible to distinguish electromagnetic component from the muonic component at the ground. The simulated N^{μ}_{max} and X_{max} at 5×10^{19}eV and at zenith angle of 38° and their dependence on mass composition of primary cosmic ray are shown in Fig. 3.2.

With these results and different possible explanations with proposed astrophysical scenarios, the main intentions for the upgrade of the Observatory were set to following:

- The main aim is to elucidate the mass composition and the origin of the flux suppression at the highest energies. Examine effects of losses due to propagation and maximum acceleration potential of sources.
- Second key objective is the search for a flux contribution of protons up to the highest energies as they could directly point to their sources.
- Lastly, the extensive air showers and hadronic interactions at the highest energies will be studied, which could help with the explanation of the discrepancy between the number of muons predicted and observed.

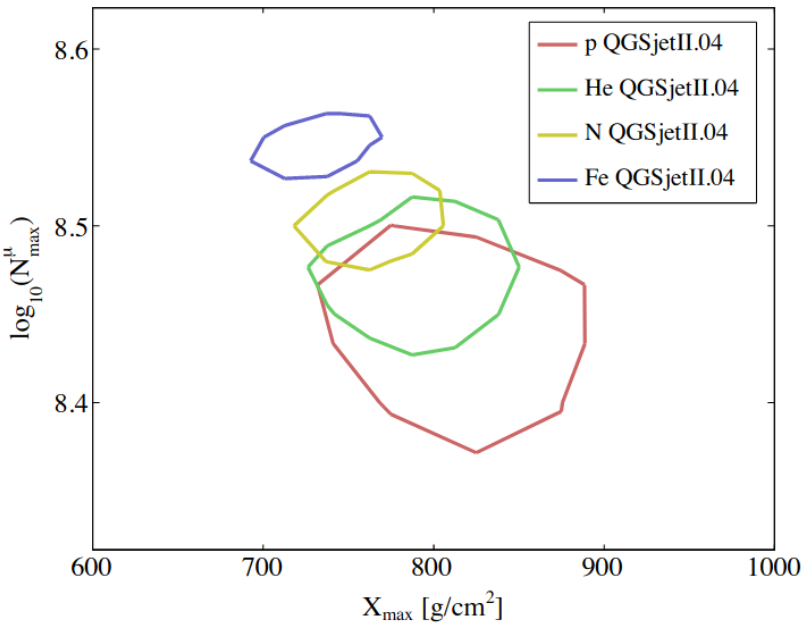

Figure 3.2: The 1σ contour of the number of muons at maximum of the muon shower development,$N^{\mu}_{\max}$, vs the $X_{\max}$ at 5×10^{19}eV and at zenith angle of 38° and their dependence on the mass composition of the primary cosmic rays [34].

3.2 Implementations of the AugerPrime upgrade

The listed goals are believed to be met by employing the following changes:

- **Scintillator surface detector**
  Thin plastic scintillator module will be deployed on each WCD station to enhance the determination of muonic and electromagnetic components of showers

- **Upgraded unified board**
  The electronics of each station will be upgraded, mainly to add channels for new detectors, but also improved with addition of ADC with faster sampling frequency and more bits

- **Underground muon detectors**
  61 muon scintillator detectors will be buried underground near to WCD stations in 750 m infill array to detect bundles of muons and their time development in a depth of 1.3 m beneath the ground

- **Small Photomultiplier Tube**
  A small PMT will be added to each WCD to extend the dynamic range even more and thus reduce the overall saturation occurrence and to study hadronic interactions closer to the shower core

- **Radio detectors**
  Radio antennas will be placed at each station to record signals from the electromagnetic component of showers

- **Extension of the fluorescence detector duty cycle**
  Duty cycle of the fluorescence detector will be increased, while lowering the PMT high voltage at the time of measurement in evenings and mornings to prevent deterioration of PMT sensitivity

3.3 Scintillator surface detector

The intention was to design a detector with 100% duty cycle that will be sensitive to different components of the air shower. The most uncomplicated way how to accomplish this, is to add an extra independent measurement to those made with the WCDs, ideally, sampled in the position of the station but with different response to different components of air shower. It should be also easy to deploy and not interrupting the ongoing detection. For these reasons, it was decided to install the plastic scintillator detector on top of each WCD station.

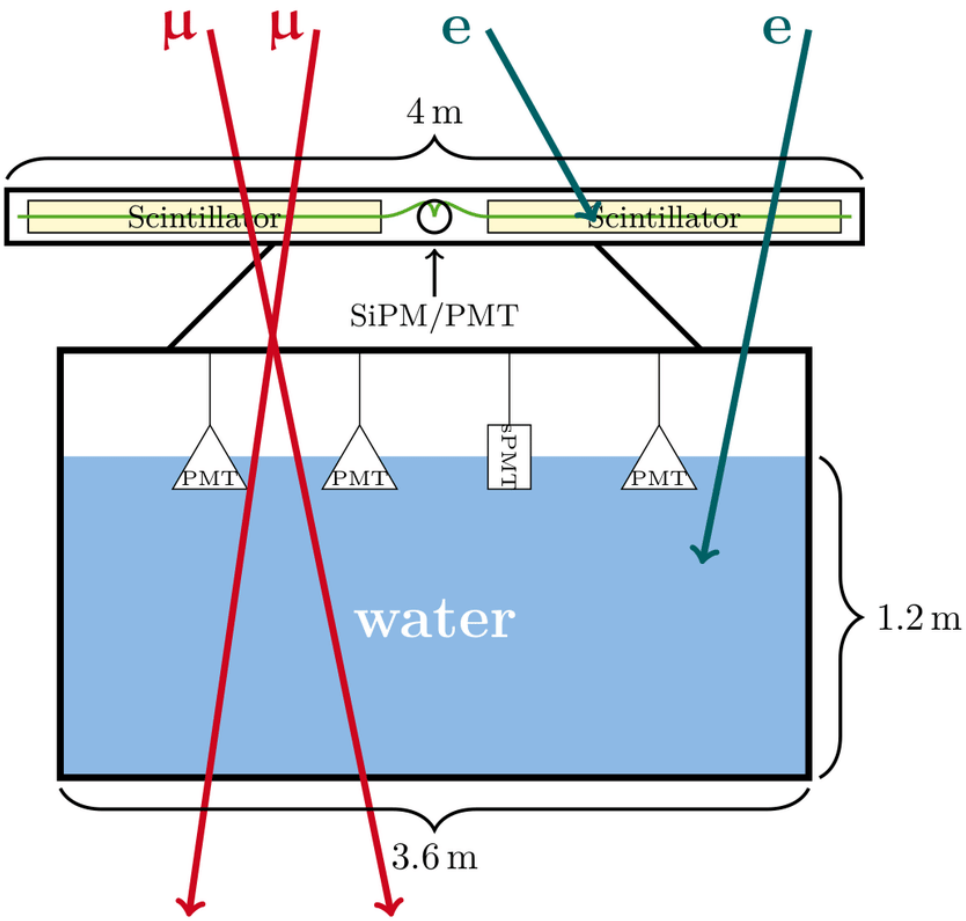

Figure 3.3: Sketch of a station of surface detector array with a scintillator detector [36].

Scintillator detector works on the scintillation process, which is a type of luminiscence. When a charged particle passes scintillation material, it can excite its molecules

and further de-excitation produces fluorescence light which is proportionate to energy of the particle.

3.3.1 Construction

The scintillator detector used in this upgrade is made of two plastic panels of $2m^2$, with wavelength shifting fibres read out by one photodetector installed between panels. Each panel has an active part consisting of 24 extruded polystyrene bars that are 1.6 m long, 1 cm thick and 10 cm wide, placed symmetrically on both sides. The bars are covered with TiO_2 mixture for higher reflectivity. The detector is enclosed in light tight aluminium cover.

Wavelength-shifting fibers are used to gather the light emitted by scintillator material and to shift the spectrum so the PMT used (Hamamatsu R9420 PMTs) has a good quantum efficiency for these wavelengths. Kuraray Y11(300)M fibers are used as the spectrum of light they absorb match the spectrum of light the scintillator emits. In Fig.3.4 are shown the emission and absorption spectra of the fibres. They measure 1 mm in diameter and are of S-type. Each fiber is placed inside two polystyrene bars separated by a 10 cm gap, with both ends connecting in the center of the SSD. There the signal is read out and similiarly as for WCD divided into two channels, with different gains, HG with the gain of 32 and LG with the gain of 1\4.

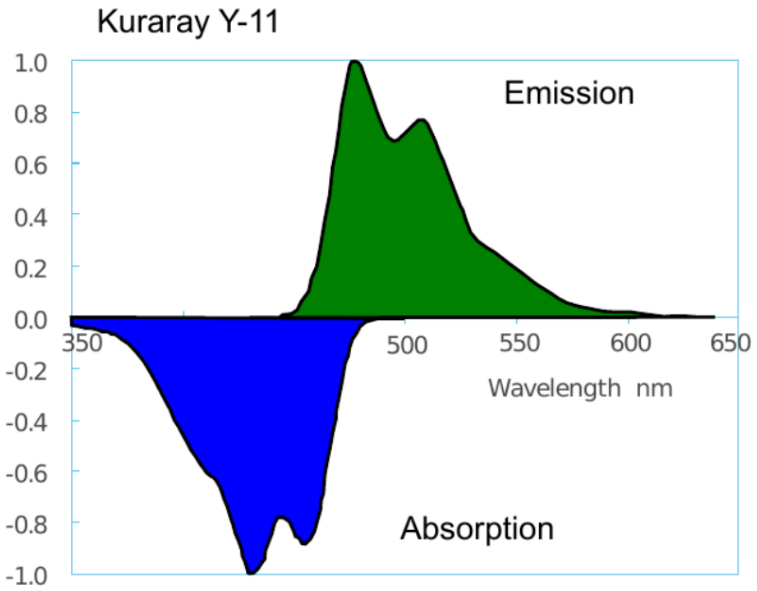

Figure 3.4: The emission and absorption spectra of Kuraray Y11(300)M wavelength shifting fibers used in SSD [34].

3.3.2 Determination of the muon component with the matrix inversion method

The muon component of a shower can be determined by using the matrix inversion method. For a detector composed of a scintillator and a water Cherenkov detector holds:

$$\begin{pmatrix} S_{\mathrm{SSD}} \\ S_{\mathrm{WCD}} \end{pmatrix} = \begin{pmatrix} \lambda A_{\mathrm{SSD}} & A_{\mathrm{SSD}} \\ \beta A_{\mathrm{WCD}} & A_{\mathrm{WCD}} \end{pmatrix} \begin{pmatrix} F_{\mathrm{em}} \\ F_{\mu} \end{pmatrix} \tag{3.1}$$

where S denotes the signal measured in MIP for SSD an in VEM for WCD, F_{em} and F_{μ} are respectively the electromagnetic and muonic flux at the ground in VEM/ m^2 and A are the horizontal areas of the SSD and WCD. β is the ratio of the horizontal WCD surface to its surface perpendicular to the zenith direction θ. and λ is the average energy left in SSD per VEM of electromagnetic flux. Using this relation we can immediately derive the equations for muonic and electromagnetic flux:

$$F_{\mathrm{em}} = \frac{1}{\lambda - \beta} \left(\frac{S_{\mathrm{SSD}}}{A_{\mathrm{SSD}}} - \frac{S_{\mathrm{WCD}}}{A_{\mathrm{WCD}}} \right) \tag{3.2}$$

$$F_{\mu} = \frac{1}{\lambda - \beta} \left(\lambda \frac{S_{\mathrm{SSD}}}{A_{\mathrm{SSD}}} - \beta \frac{S_{\mathrm{WCD}}}{A_{\mathrm{WCD}}} \right) \tag{3.3}$$

The results of simulations have shown, that parameters λ and β have almost no dependence on the chemical composition of a primary particle and also on hadronic interaction models. From this we can reconstruct the muon signal in WCD by:

$$S_{\mathrm{WCD},\mu} = A_{\mathrm{WCD}} F_{\mu}. \tag{3.4}$$

Obtained number of muons will be cross-checked with the measurement of the Underground Muon Detectors of AMIGA. These detectors provide direct measurement of muons in an independent way, nevertheless, due to a layer of soil above them, the energy threshold of muons they are able to detect is higher than for the combination of the SSD and the WCD.

Chapter 4

Surface detector data processing and event reconstruction

4.0.1 SD triggers

For correct identification of events, each station must meet certain criteria. This is accomplished by the chain of triggers [20]. The main trigger is the shower trigger, which comprises two levels. The first trigger is called T1 trigger and is used to distinguish between the background signal and events of interest to the Observatory. It holds two separate modes.

- Threshold trigger (TH). Requires coincidence of all (three) PMTs with signal more than 1.75 VEM. This trigger selects large signal and therefore is useful for the detection of inclined showers, that are mostly muonic.
- Time over threshold (ToT). At least two PMTs measure signal more than 0.2 VEM for more than 13 time bins in a time window of 120 bins. This trigger selects low signals spread in time. It is effective for close, low energy showers (mainly electromagnetic) or for distant high energy showers.

The next trigger level is called T2. TH for T1 must require 3.2 VEM threshold to pass the T2-TH and T1-ToT are automatically promoted to T2-ToT.
Passing T2 trigger level, a station sends the signal to the Cental Data Acquisition System (CDAS) to decide if data will be stored as an event. This is done by next, global trigger T3, that also posses two modes of different spatial criteria.

- Signal must pass T2-ToT and coincidence of at least three stations is required, where at least one must be of the nearest neighbours and one may be of the second nearest neighbours, this trigger is called "$ToT2C_1\&3C_2$"(C_n symbolises $n-th$ set of neighbours).
- The second criteria requires passing one of the T2 triggers and coincidence of four stations, where the remaining station must be up in a fourth set of the nearest neighbours. This trigger is called "$2C_1\&3C_2\&4C_4$" and is useful for horizontal showers, that leave wide spread signal on the ground.

The spatial criteria for T3 triggers are shown in Fig. 4.1.

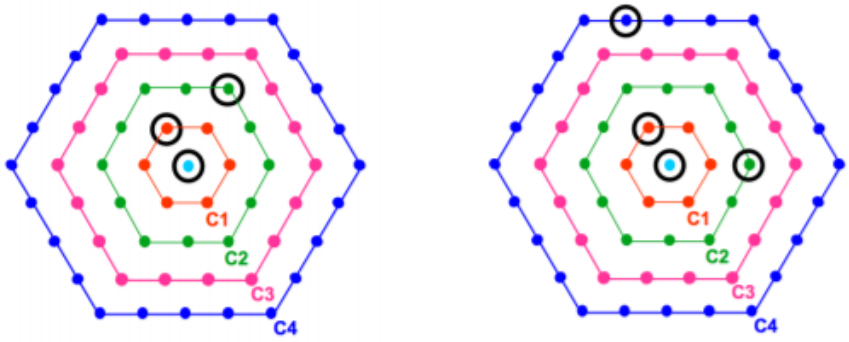

Figure 4.1: Example of T3 spatial criteria. Left: The 3-fold T3 mode $ToT2C_1\&3C_2$. Right: The 4-fold mode $2C_1\&3C_2\&4C_4$. C_n symbolises $n-th$ set of neighbours [20].

The next level trigger T4 is used to more precisely differentiate between events of interest (showers) and unwanted, accidental events and it is comprised of two modes.

- The first mode T4-3ToT, requires fulfilment of the T2-ToT trigger for three nearby stations that lay in a triangle.
- The second mode T4C1 requires fulfilment of one of the T2 triggers for four stations, where three stations must lay in a hexagon of the closest neighbours to a fourth station. It also requires that the signal time corresponds to a plane shower front moving at the speed of light.

Both configurations are shown in Fig. 4.2.
Next trigger called T5 is mainly used for the bordering stations, where a part of a shower can be lost [20].

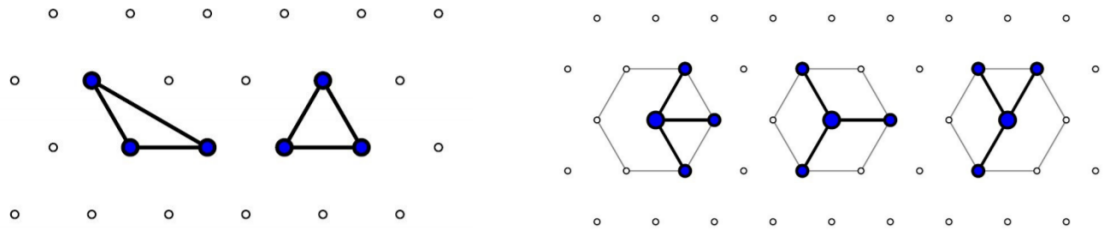

Figure 4.2: The spatial critera for T4 trigger. T4-3ToT configuration of stations is on the left and T4C1 is on the right [21].

4.0.2 Surface detector calibration

The digitized traces of signal recorded by WCD must be calibrated to provide a common reference level between different tanks. The calibration of the SD is performed

locally by each station electronics. It is convenient because of the large number of the stations, the limited bandwidth for the data transmission to the central acquisition system (1200 bits per second) and the differences between each station.

Atmospheric muons are used as a source for calibration, as they pass the station with the rate of 2500 Hz [16]. The average charge that is produced by a muon vertically traversing the tank - VEM (Vertical equivalent muon) is used as a reference unit in the Observatory. The signal recorded by WCD PMTs are therefore converted into VEM units. The aim of this calibration is to measure the value of 1 VEM in hardware units (integrated FADC channels). The calibration proceeds as follows.

From the one minute worth sample of background signal measured just before the recorded event by the WCD, the calibration histograms for each PMT are generated. The "charge" histogram, which is created from the integrated pulses in the trace, then the histogram of pulse heights and the baseline histogram. The position of the second peak in a charge histogram is fitted and the bin containing the peak is defined as a Q_{VEM}.

To confirm the position of the second peak, truly vertical and centered muons were measured in a setup with scintillators above and under the station. When compared, it was found out, that the obtained value from fitting of histograms must be rectified by a correction factor, as the peak is slightly shifted (see Fig. 4.3), $Q_{\mathrm{VEM}} = 1.09$ VEM.

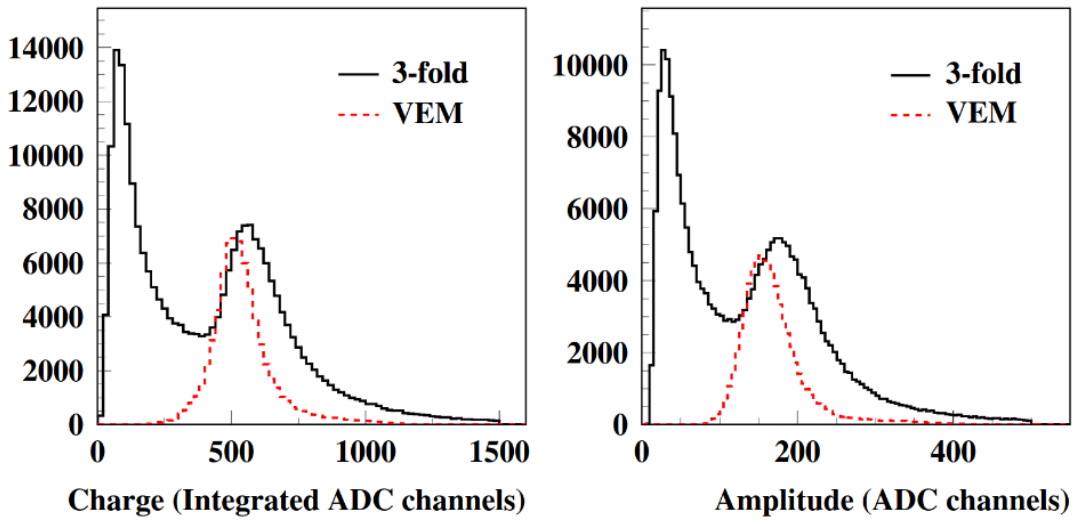

Figure 4.3: The charge and the pulse height histogram for background signals with the second peak showing the muon signal. The red lines represent truly vertical and central muons [16].

Similarly we define I_{VEM} as the bin containing the peak in the pulse height histogram. This value is used for triggering as it provides a reference amplitude, however, it is not determined online as VEM because it would cause large dead times of the detector. Instead, its value is tuned until the trigger rate of the detector reach 70 Hz.

The first peak in both histograms is formed by particles that deposit low energy in water e.g. electrons, gammas, short track muons...[17]. To further understand the interpretation of the peaks in the histograms, we must take into consideration the following. When a muon passes a tank, three situations can occur. The muon can: [18]

1. Enter the detector through the top and get out through the bottom
2. Enter through the top or the bottom end get out through the side
3. Enter through the side and get out through the side

Distributions for each possibility and their sum are shown in Fig.4.4. The VEM is obviously the peak created in the first situation. The charge histogram then can be interpreted as the convolution of the mentioned distributions [18].

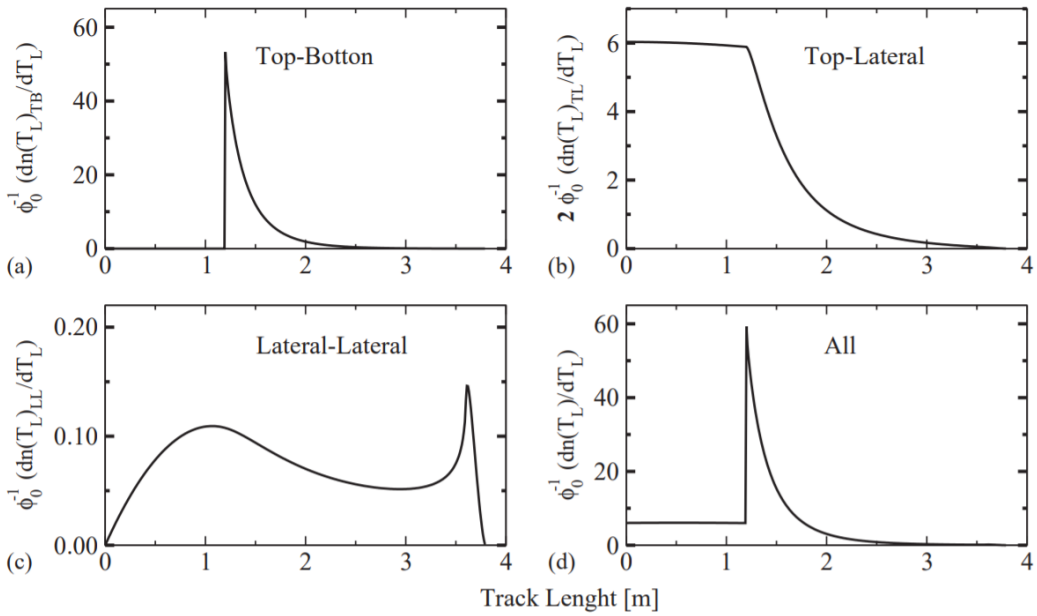

Figure 4.4: Distribution of track length of traversing muon that a) enters through the top and gets out through the bottom, b) enters through the top and gets out through the wall c) enters and gets out through the wall and d) sum of all [17].

Summarizing, the calibration has three main steps:

- Set up the overall gain of each PMT to have I_{VEM} at 50 FADC counts (updated regularly)
- Continually perform the online calibration to determine I_{VEM} to adjust the electronics level trigger which compensates the shift in the first step
- Determine the value of Q_{VEM} from the charge histograms, and convert the integrated signal to VEM units using $Q_{\mathrm{VEM}} = 1.09$ VEM.

After conversion of the recorded signal of each PMT in station into VEMs, the complete signal of the station is acquired as the average of the signals [19].

4.0.3 Calibration of SSD

The SSD is triggered by WCD and calibrated similiarly as WCD, but instead of VEM, the scintilator is measuring signals from the minimum ionizing particles - MIP. The signal of a MIP corresponds to $\sim$ 12 photoelectrons (VEM in WCD $\sim$ 64 pe), so it can be easily lost in background, that is why the cross-trigger with WCD is used. Compared to WCD, the scintillator detector will trigger $\sim$ 40% of the calibration triggers of the WCD [37]. MIP charge is analogically determined from charge histograms by fitting the second peak.

A new mode of the SSD MIP signal triggered in coincidence with the WCD VEM signal for the detector calibration is currently being developed.

4.0.4 SD event reconstruction

SD detectors measure the signal from the Cherenkov light inside the station and arrival time to the station. From these quantities, it is possible to determine the shower geometry, its size and the arrival direction of the primary cosmic ray.

Shower geometry

As each triggered station measures the start times of the signal t_i, it is possible to determine the arrival direction of a shower by fitting them to a front of a plane. The shape of the front is approximated by a sphere, expanding with a speed of light. The measured time of such a shower front at a point $\vec{x_i}$ (positions of the stations) can be expressed as

$$c(t_i - t_0) = |\vec{x}_{\mathrm{sh}} - \vec{x}_i|, \tag{4.1}$$

where $\vec{x}_{\mathrm{sh}}$ is a virtual origin of the shower development at the time t_0. By this fit the place were the core of the shower hit the ground $\vec{x}_{\mathrm{c}}$ is determined. The distance between the virtual origin of a shower and the point, where it hit the ground is the radius of a curvature of the sphere

$$R_0 = |\vec{x}_{\mathrm{sh}} - \vec{x}_{\mathrm{c}}|. \tag{4.2}$$

Lateral distribution function

The lateral distribution function (LDF) describes the dependence of the signal at the ground on the distance from the shower core. This function can be written as

$$S(r) = S(r_{\text{opt}}) f_{\text{LDF}}, \tag{4.3}$$

where f_{LDF} is a modified Nishimura-Kamata-Greisen function

$$f_{\text{LDF}} = \left(\frac{r}{r_{\text{opt}}}\right)^{\beta} \left(\frac{r + r_1}{r_{\text{opt}} + 1}\right)^{\beta+\gamma}, \tag{4.4}$$

where r_{opt} is the optimum distance which was estimated to be 1000 m for the main array, $r_1 = 700$ m, $S(r_{\text{opt}})$ is the estimated signal at the optimum distance, β and γ are fitted parameters.

The WCD records the signal from Cherenkov light that is generated by different particles. Therefore, it is almost impossible to determine the number of particles that have passed through the tank. To fit the LDF, we must first convert the signal in VEM units to the effective particle number. 1 VEM is converted into one particle as a mean signal of a muon. The effective particle number is given by:

$$n = pS, \tag{4.5}$$

where p is Poisson factor defined as:

$$p = \max(1, f_{\text{S}}^{-2}(\theta)) \tag{4.6}$$

and $f_{\text{S}} = 0.32 + 0.42 \sec(\theta)$ represents the uncertainty on the signal. The shower size S(1000) is obtained by the LDF fit to the station signals using the maximum likelihood method:

$$\mathcal{L} = \prod_i f_{\text{P}}(n_i, \mu_i) \prod_i f_{\text{G}}(n_i, \mu_i) \prod_i F_{\text{sat}}(n_i, \mu_i) \prod_i F_{\text{zero}}(n_i, \mu_i), \tag{4.7}$$

where n_i is the detected effective particle number for each station and μ_i its expectation. Each station contributes to the function differently by the recorded type of signal:

- Small signals described by Poisson probability distribution

$$f_{\text{P}}(n_i, \mu_i) = \frac{\mu_i^{n_i} e^{-\mu_i}}{n_i!} \tag{4.8}$$

  .

- Large signals described by Gaussian probability distribution

$$f_{\text{G}}(n_i, \mu_i) = \frac{1}{\sqrt{2\pi}\sigma_i} \exp\left(-\frac{(n_i - \mu_i)^2}{2\sigma_i^2}\right), \tag{4.9}$$

  where σ_i is obtained from the signal uncertainty model.

- Saturated signals which can not be recovered are described as lower limit and thus calculated as the integral of the Gaussian probability distribution for $n>n_i$

$$F_{\text{sat}}(n_i, \mu_i) = \int_{n_i}^{\infty} f_{\text{G}}(n, \mu_i) = \frac{1}{2}\text{erfc}\left(\frac{n_i - \mu_i}{\sqrt{2\sigma_i}}\right), \tag{4.10}$$

  where erfc is compelementary error function.

- Zero signals for non-triggering stations are described as a sum over all Poissonian probabilities for $n_i<n_{\text{th}}$, where n_{th} is threshold number of particles for station to trigger (approximately 3).

$$F_{\text{zero}}(n_{\text{th}}, \mu_i) = \sum_{n=0}^{n_{\text{th}}} f_{\text{P}}(n, \mu_i). \tag{4.11}$$

  The actual fit of LDF is done by minimizing the negative logarithm of the likelihood function 4.8, because it is easier to fit a sum of functions than a product.

Shower arrival direction

After obtaining the virtual shower origin $\vec{x}_{\text{sh}}$ and the impact point $\vec{x}_{\text{gr}}$ (where the shower hits the ground, obtained from LDF), the shower axis $\hat{a}$ can be determined as:

$$\hat{a} = \frac{\vec{x}_{\text{sh}} - \vec{x}_{\text{gr}}}{|\vec{x}_{\text{sh}} - \vec{x}_{\text{gr}}|}. \tag{4.12}$$

Chapter 5

Calibration of Surface detector

For analysis in this chapter, various data and software tools were used. For plotting the histograms for stations in the pre-production array and studying the long-term evolution of VEM and MIP I used the ADST PPA_SDRec_*.root data and the Offline software. For plotting the histograms for stations with new electronics and comparison of histograms before and after addition of SSD I used raw sd_*.root data.

5.1 Calibration histograms

As mentioned before, during the calibration procedure, the station sends histograms together with event data to the CDAS. In order to further understand calibration, I drew the calibration histograms for chosen stations.

For the detectors from the pre-production array with old electronics, the data are stored within the ADST, the structure, which is comprised of root based variables used for event reconstruction at the Pierre Auger Observatory. The calibration histograms can be obtained by combining separate values on the content of bins and binning of the histograms. I prepared the charge histograms for station 1755 in Fig. 5.1, and for 909 in Fig. 5.2.

These stations have old electronics, thus the charge histograms contain data for the two of WCD PMTs and for the PMT connected to the scintillator detector.

It can be seen, that for each station the histograms are different. This is caused mainly by different properties of the tanks, for example by the water quality or the reflectivity of the Tyvek liner. In Fig. 5.2, there are also visible differences between PMTs in the same station, this is due to the slight variation in properties of PMTs like the high voltage. Both histograms exhibit two expected characteristic peaks, the second corresponds to VEM as it was explained in 4.0.2.

The charge histogram of the SSD is visibly distinctive from the others, mainly by the height of the first peak. This peak, unlike in WCD histograms, represents the integrated baseline fluctuations. This is caused by triggering SSD by signal recorded

in WCD, and thus there is contribution from events that have crossed the WCD, but not the SSD.

The calibration histogram information for the stations with UUB had to be extracted from the raw data files. In these files, the data for each histogram are stored as the values of its bin centers, bin widths and bin contents. Combining this information I drew the charge histograms for station 22 in Fig. 5.3 and for station 39 in Fig. 5.4.

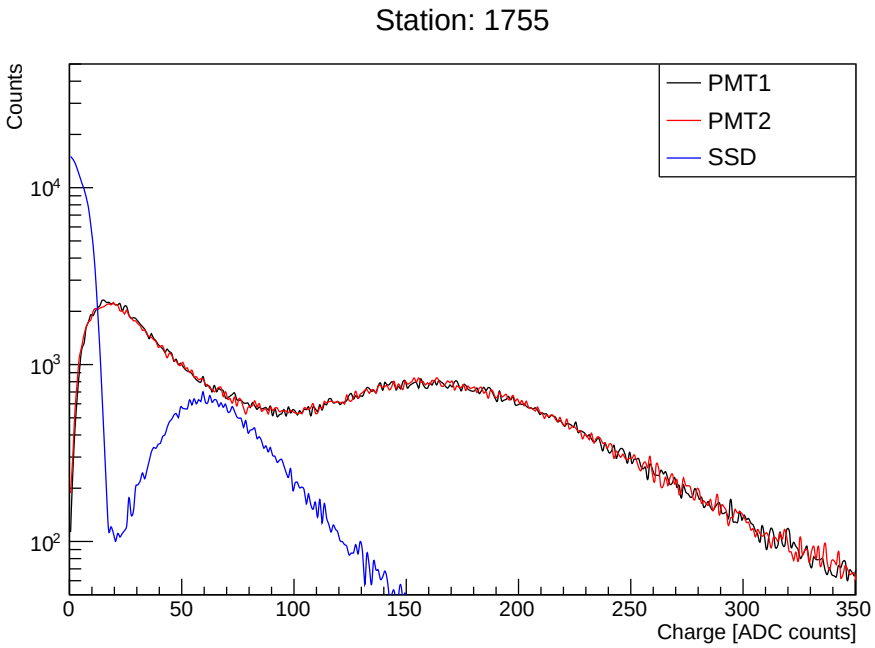

Figure 5.1: Charge calibration histogram from station 1755.

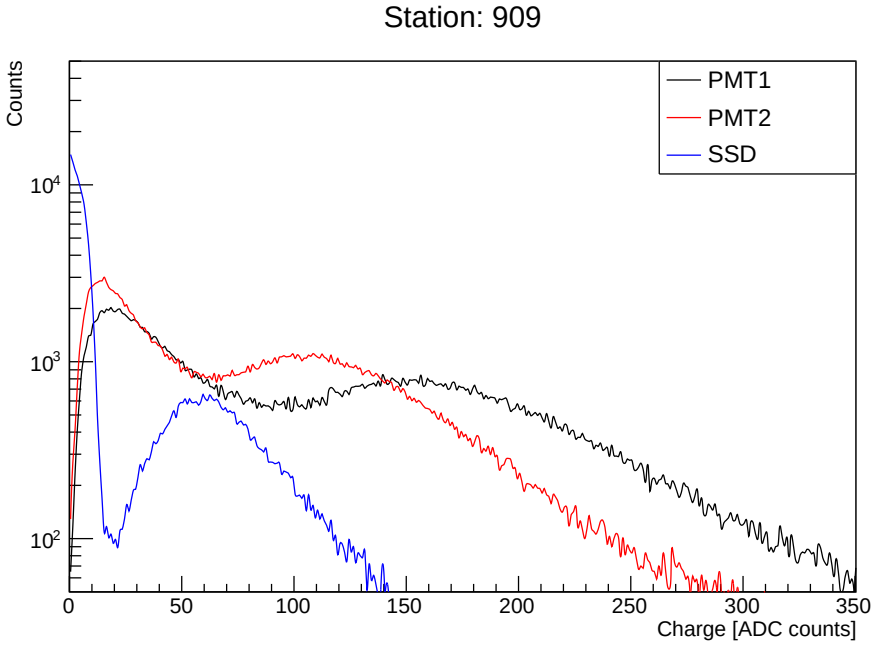

Figure 5.2: Charge calibration histogram from station 909.

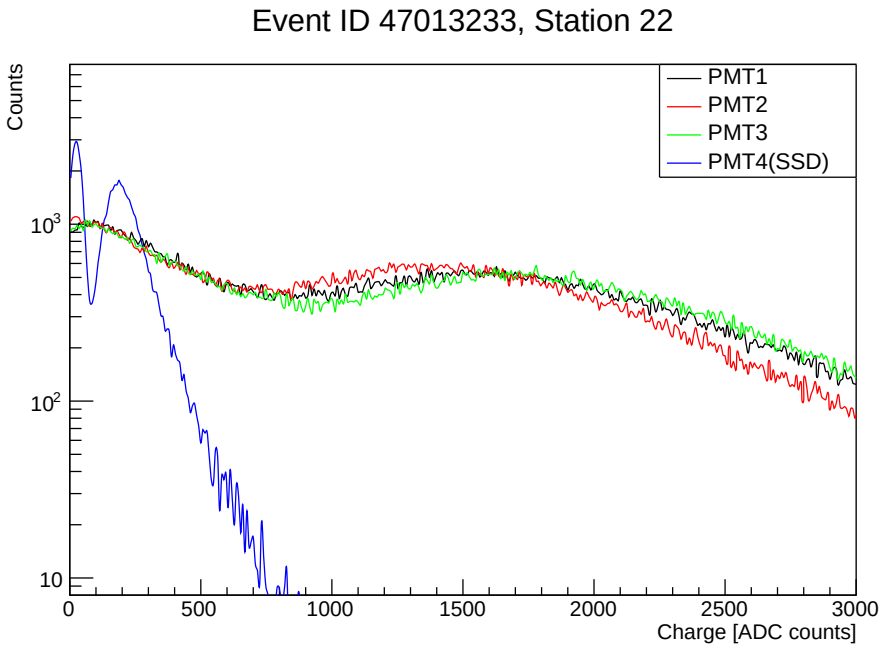

Figure 5.3: Charge calibration histogram from station 22.

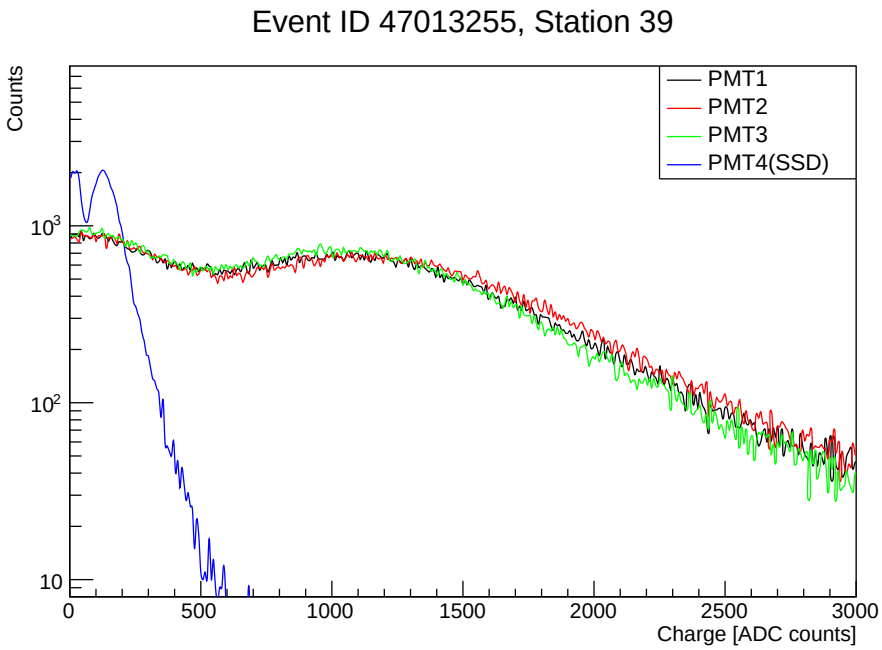

Figure 5.4: Charge calibration histogram from station 39.

These histograms contain data from all of the three WCD PMTs and also from the SSD PMT. Slight differences between the stations and the PMTs are visible too.

5.2 Long-term evolution of VEM and MIP

To understand the effects of the scintillator on calibration and also to study the response of the detector, it is useful to examine a long-term evolution of VEM and MIP. The scintillator detector was implemented in March 2019, so the time span the VEM was examined was chosen to depict some period before and after the implementation. The values of VEM and MIP charge are available in ADST. I plotted the evolution of VEM charge for station 663, PMT 1, which is depicted in Fig. 5.5 and also for station 847, which is in Fig. 5.6.

In both figures we can see a common trend in the increase of the value of VEM charge during the winter months. This feature is due to seasonal modulations, most probably linked to temperature variation in the atmosphere. Different temperatures cause changes in the water density, and therefore in recorded Cherenkov photons. The amplitude of this modulation is different for all stations and is due to differences in electronics [39]. Overall, any significant change in VEM charge value after addition of SSD is not convincingly proved.

In the 5.7 and 5.8 are shown evolutions of MIP charge for stations 663 and 919, from the time SSD was installed. It is visible, that MIP is less affected by seasonal changes than VEM.

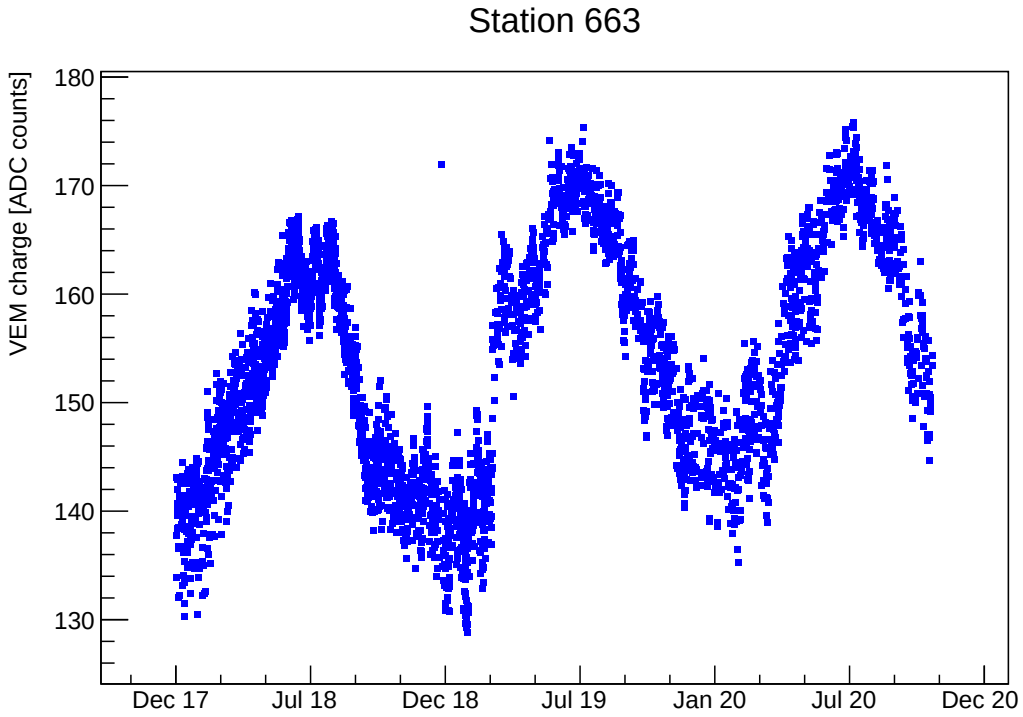

Figure 5.5: VEM charge evolution during years 2018 to 2020 for station 663.

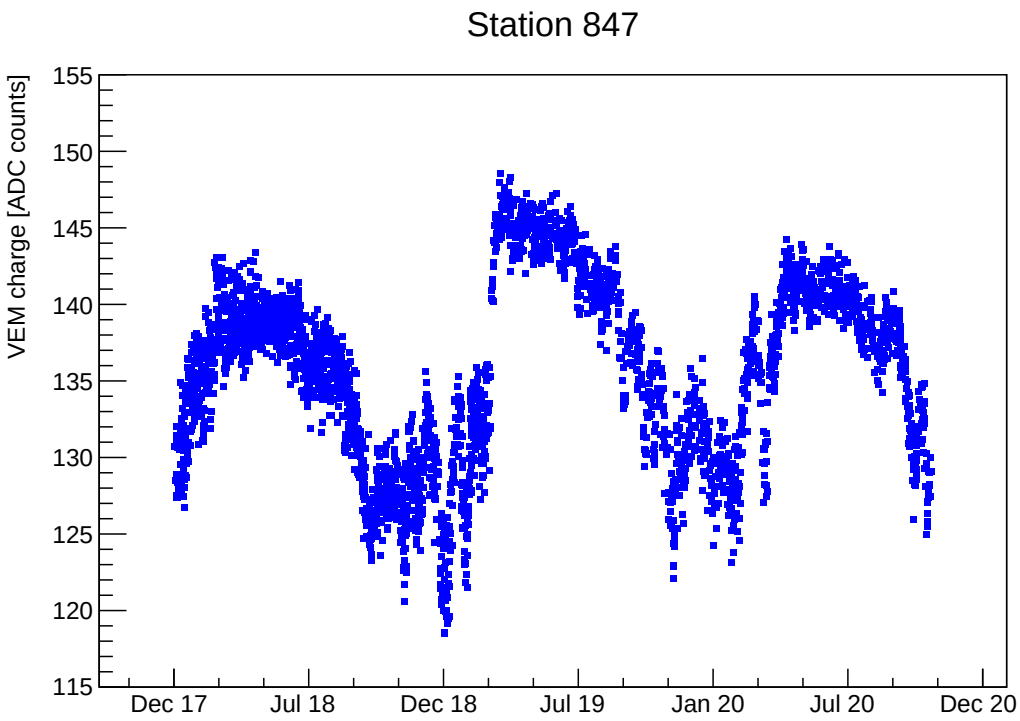

Figure 5.6: VEM charge evolution during years 2018 to 2020 for station 847.

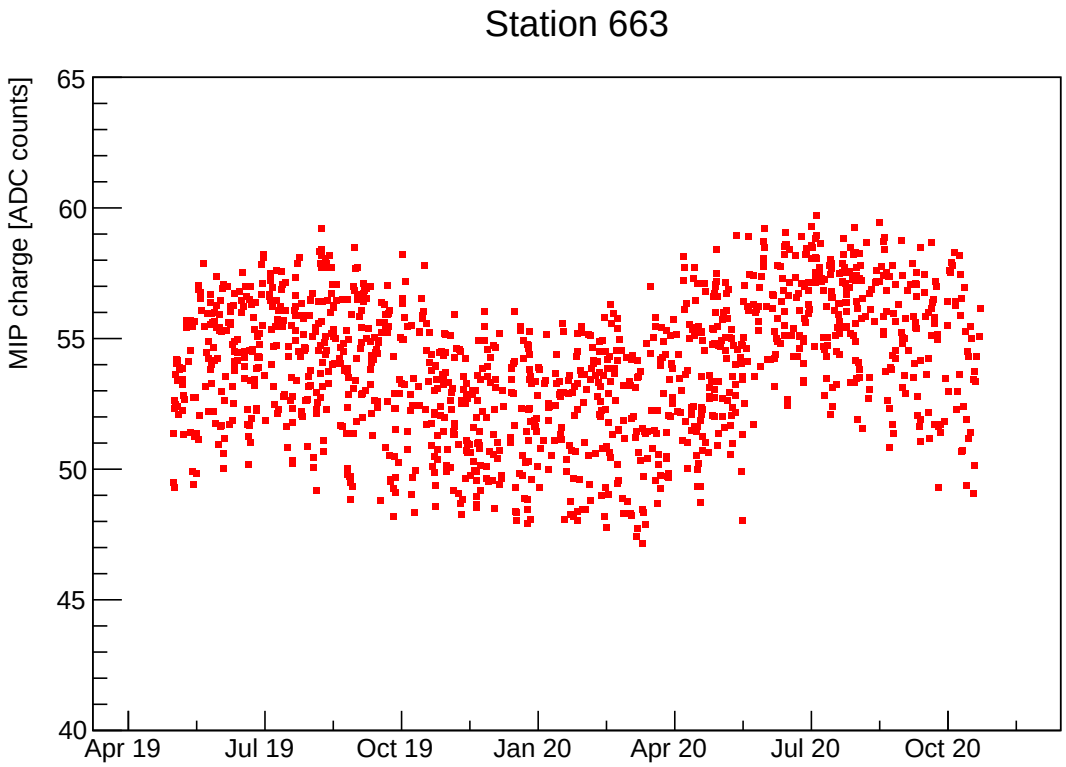

Figure 5.7: MIP charge evolution during years 2019 to 2020 for station 663.

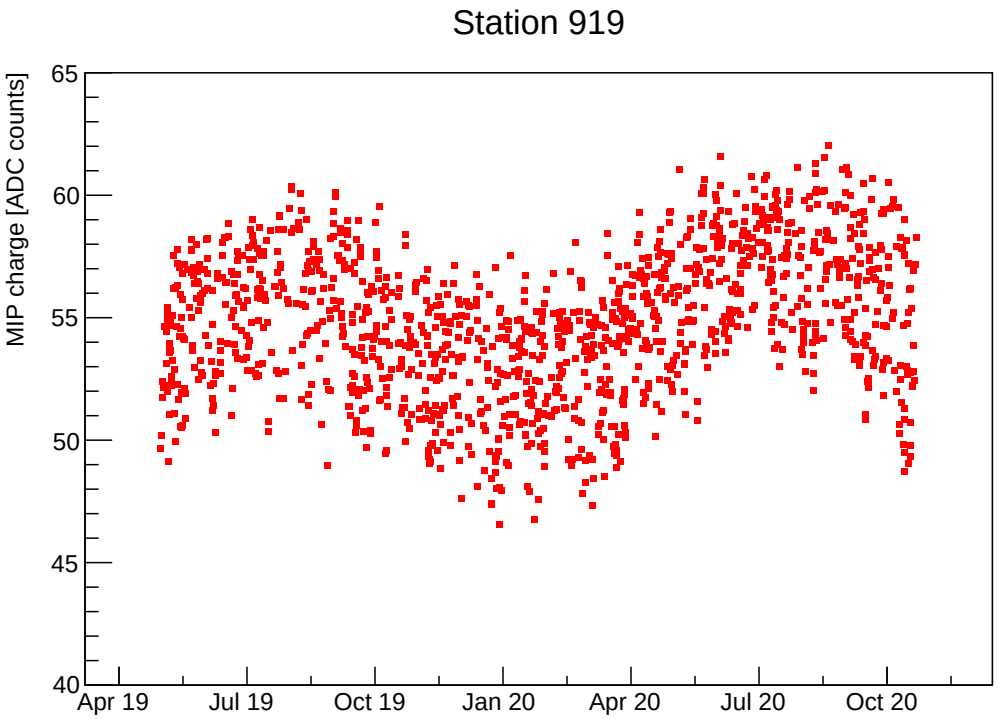

Figure 5.8: MIP charge evolution during years 2019 to 2020 for station 919.

5.3 Change of the histograms after adding SSD

Although any unusual change of VEM charge after adding SSD was not confirmed by the study of evolution, the calibrations histograms could have changed. These changes can have informative value on how the detector behaves.

Therefore, I tried to examine charge histograms themselves before and after addition of SSD.

To truly obtain the change in the histograms as a result of added detector not contaminated by other effects such as aging or seasonal modulation, I decided to look at the data from the end of February 2019 and the end of March 2020, because during March, the SSDs were being implemented in stations chosen for this analysis.

The histograms from February and March were examined for three different stations (663, 847, 919) from the pre-production array. These stations have old electronics and thus only the two of the WCD PMTs were connected. For them, I plotted the histograms, the results are shown in Fig. 5.9.

If we inspect these histograms, it is obvious that they exhibit one common feature, and that is the growth of the first peak after addition of the scintillator detector.

The shift of the muon peak in some plots signifies, that the gain of PMTs was changed and they were recalibrated. This caused the change of the threshold trigger and therefore affected the first peak. This change is thus not caused by any contribution in the electromagnetic component of shower. For the calibration of the shower signal,

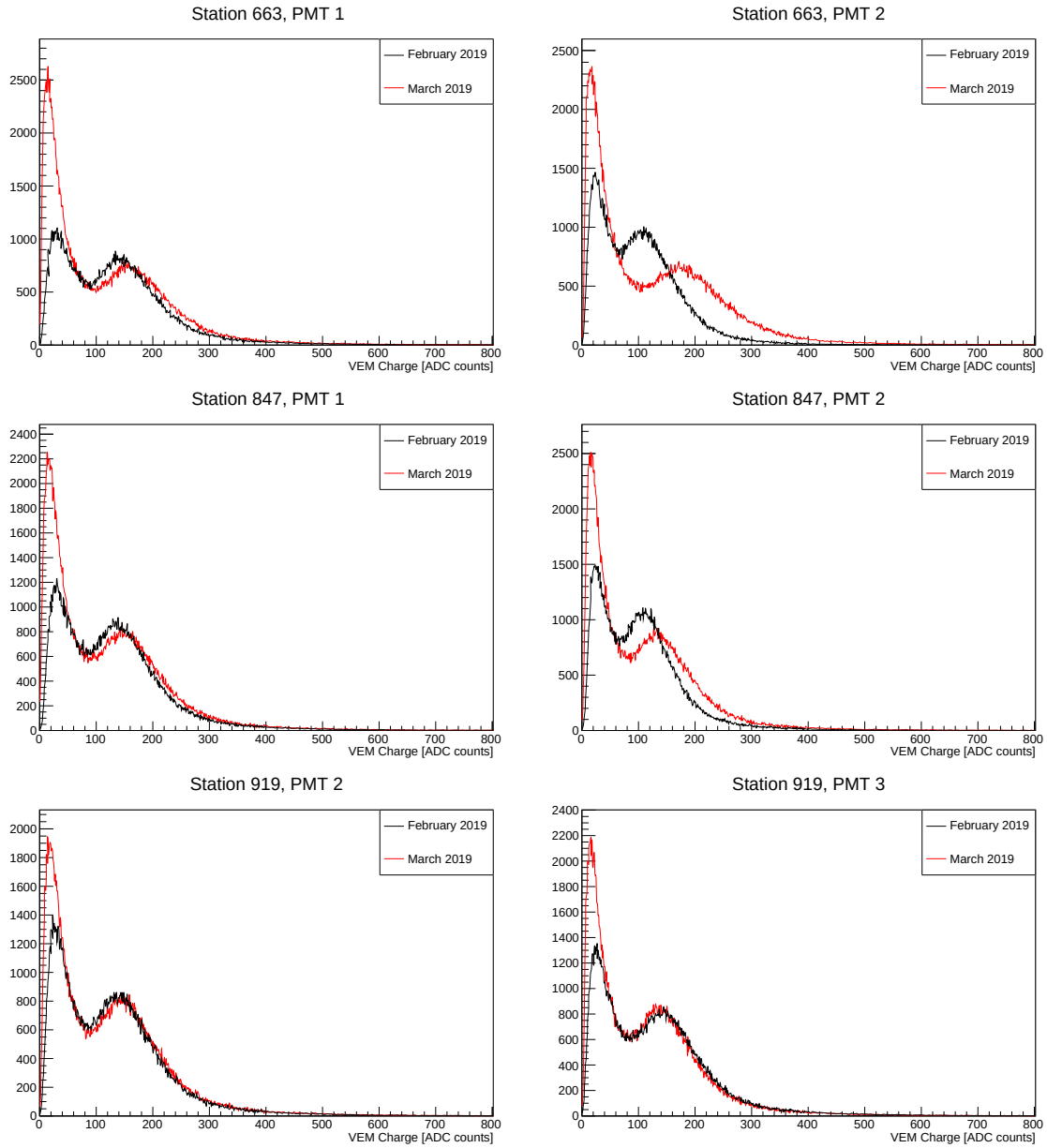

Figure 5.9: Charge calibration histograms for three different stations before addition of SSD (black) and after (red).

the used value is obtained from a one minute sample just before the event and thus the changes of both gain and the threshold are taken into concern.

5.4 Coincidence with SSD

A new approach for the detector calibration using the SSD MIP signal triggered in coincidence with the WCD VEM signal is being studied in the Long term performance task. The main motivation for changing the method of calibration is due to the fact, that the older the detector, the less clear the muon peak in the calibration

histogram. This is caused by the various effects like decrease of the reflectivity of the diffusive liner, reduced efficiency of PMTs and the absorption of Cherenkov light in the water, called the aging of the detector [38]. An example of the impact of the detector aging on the identification of the peak is shown in Fig. 5.10. The calibration histograms were prepared for the station 919, for years 2005 and 2019 respectively.

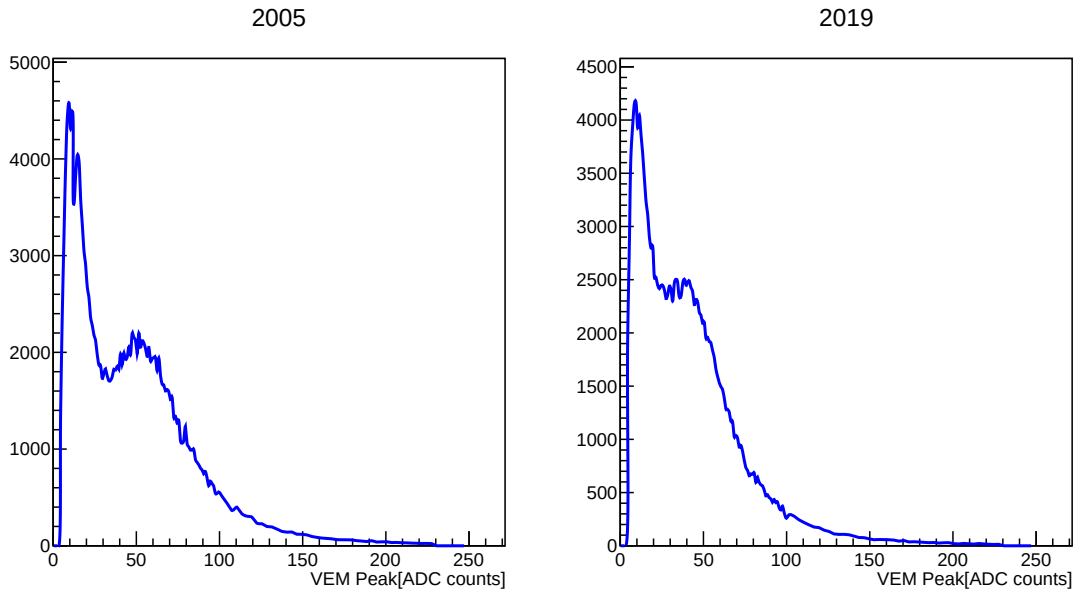

Figure 5.10: Calibration histograms for station 919, in 2005 and 2019.The identification of the peak is due to aging of the detector more difficult.

To study the new method of the WCD calibration with the coincidence with the SSD, special data from WCD are needed, as the stations are sending complete calibration histograms to CDAS and no individual values of variables. The data used in this analysis were taken specially for the station 22 "Trak", which is located in the infill array and has new electronics (UUB).

The data contain separate values of charge and peak obtained from the muon traces from calibration. At first, I made histograms from the charge values and from the peak values, respectively. They are shown in Fig. 5.11.

We can see both peaks in each histogram, with the first peak being the more prominent one. As it was mentioned before, VEM should correspond to signal left by muon vertically traversing the tank, but actually, the value that we determine as one VEM is sligthly shifted to real VEM. To reduce this error, we can use the SSD signal to filter out events with smaller zenith angle and the VEM peak will be enhanced.

I selected WCD peak and charge data with the plain condition for the SSD peak to be more than 10 FADC counts. This condition represents the criterion to choose only vertical particles, that passed through SSD. Then I made histograms from these selected data. The obtained results are depicted in Fig. 5.12. It is visible, that electromagnetic background was reduced, the first peak is much smaller and the VEM peak is better identified in both histograms.

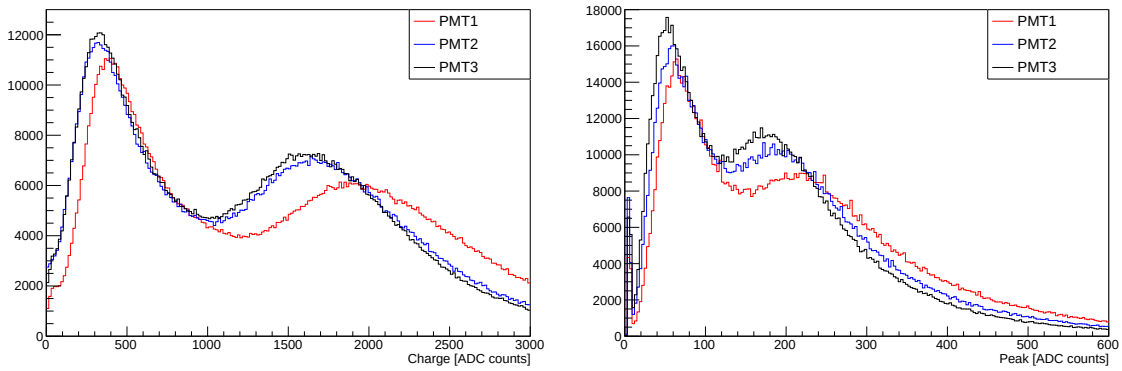

Figure 5.11: Left: Charge histogram for station 22 "Trak". Right: Peak histogram for station 22 "Trak"

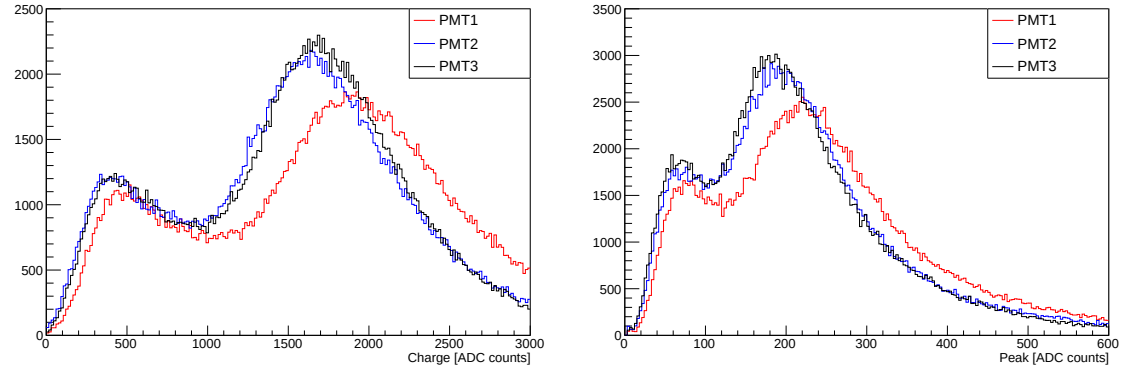

Figure 5.12: Left: Charge histogram for station 22 "Trak". Right: Peak histogram for station 22 "Trak". Values chosen with coincidence with SSD.

5.5 The Baseline and the noise of the UUB

The implementation of the final version of the V3 UUB started in the end of November 2020. It is in the utmost interest to confirm that the eletronics work how it was expected to. I studied the variation of the baseline and the noise of the high gain channel with temperature. The HG channel was chosen, because due to the higher gain, it has larger noise compared to the low gain channel. I processed data from the beginning of December 2020 to the 20th of January 2021. The temperatures during this time were taken from the CLF.

I computed the baseline B as the average value of the first 300 bin contents x_i in the event trace, as these bins should contain only background noise and no shower signal,

$$B = \frac{1}{N} \sum_{N} x_i. \tag{5.1}$$

To visualize the changes in the baseline with temperature I plotted the baselines together with temperature in the examined month for station 1729, the WCD PMT

1, which is in Fig. 5.13 and also for the SSD PMT, which is in Fig. 5.14.

The noise was calculated as the root mean square σ_{RMS} of the first 300 bins in the trace,

$$\sigma_{\mathrm{RMS}} = \sqrt{\sum_{N} \frac{(x_i - B)^2}{N}}, \tag{5.2}$$

and also plotted together with temperature. The results are in Fig. 5.15 for the WCD PMT 1 and in Fig. 5.16 for the SSD PMT. For the PMT 1, the average baseline value was computed to be $B = (244.4 \pm 0.6)$ ADC counts, and for the SSD PMT, $B = (231.9 \pm 0.9)$. The determined value of noise for SSD is $N = (1.96 \pm 0.14)$ ADC counts, and for the WCD PMT 1, $N = (1.97 \pm 0.15)$ ADC counts. Temperature had average value of $(19 \pm 7°\mathrm{C})$. Considering the difference between the highest temperature during the day and the lowest during the night, which was approximately 21°C, the baselines did not show any significant changes or temperature dependence. Unfortunately we do not have enough data to be assured about the examined behaviour of the UUB, as it was deployed only at the end of year 2020.

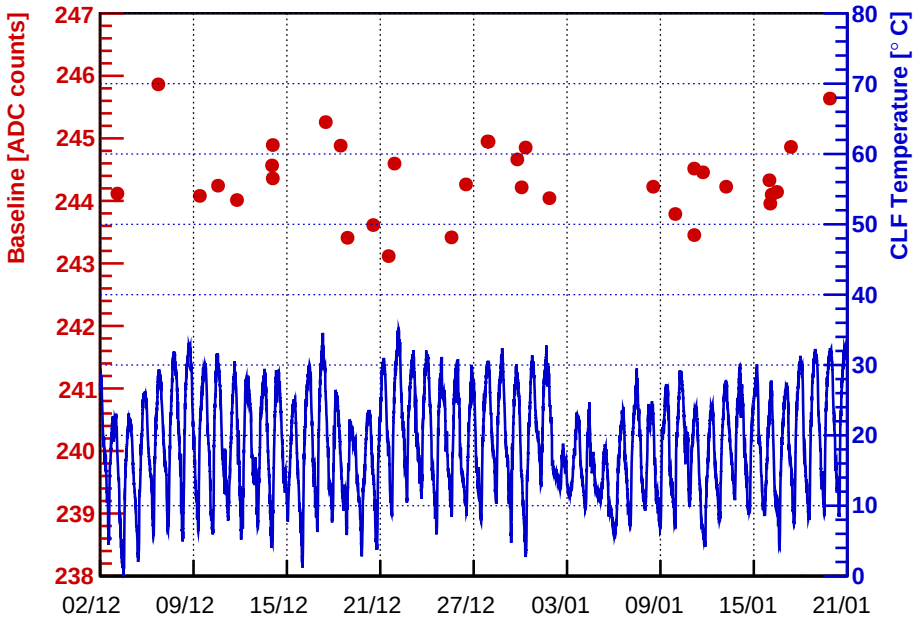

Figure 5.13: The baseline of the WCD PMT 1 for station 1729 together with temperature in time. Data taken from the beginning of December 2020 to the 20th of January 2021.

5.6 Gain ratio of channels with high and low gain

The gain ratio between high gain and low gain channel was designed to be 32 to achieve good dynamic range. In reality, due to differences in electronics, this value

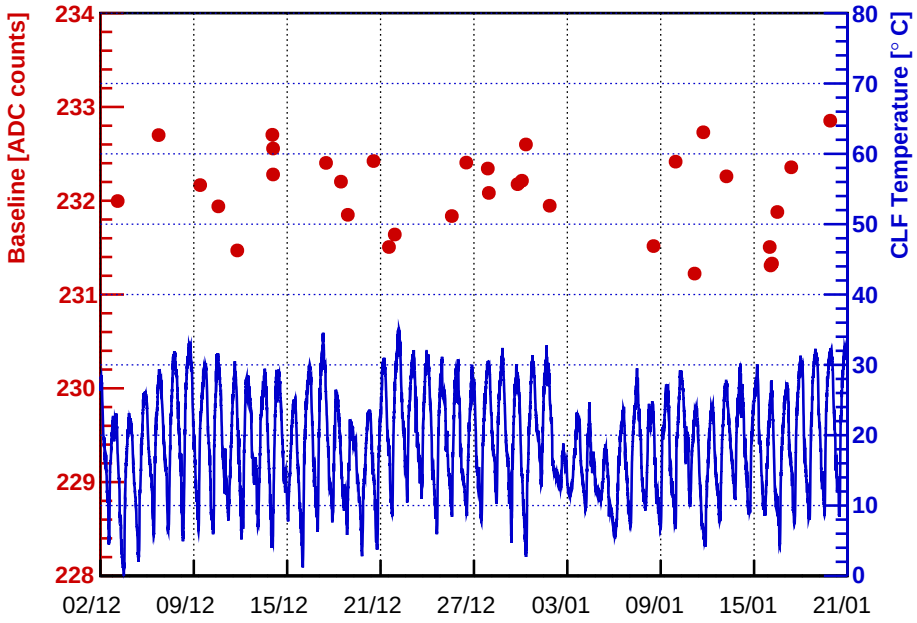

Figure 5.14: The baseline of the SSD PMT for station 1729 together with temperature in time. Data taken from the beginning of December 2020 to the 20th of January 2021.

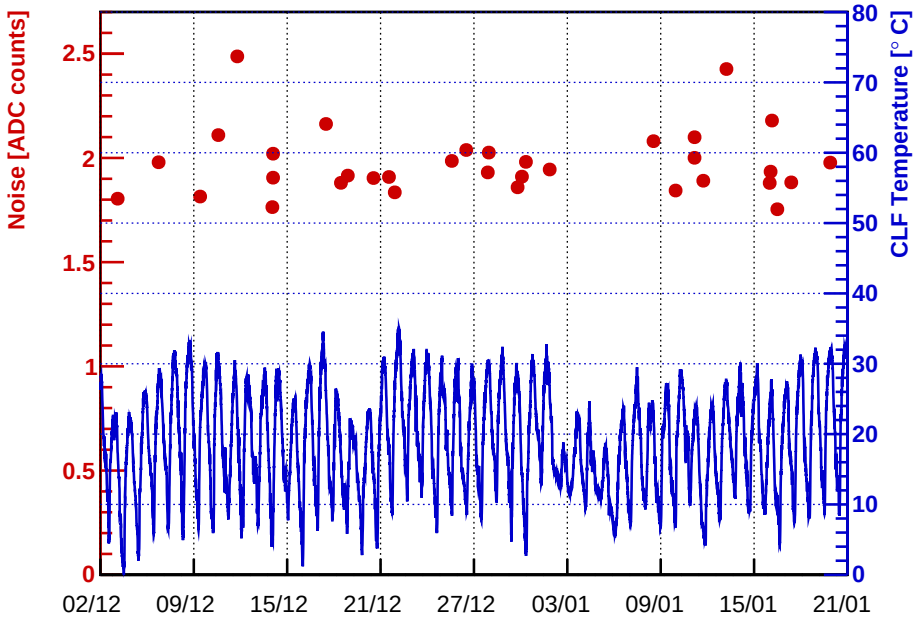

Figure 5.15: The noise of the WCD PMT 1 for station 1729 together with temperature in time. Data taken from the beginning of December 2020 to the 20th of January 2021.

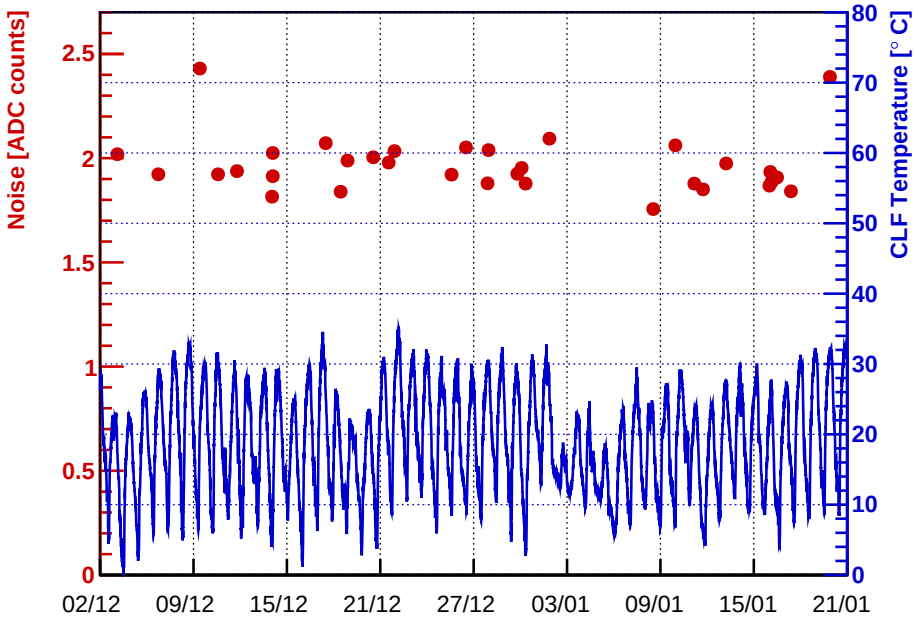

Figure 5.16: The noise of the SSD PMT for station 1729 together with temperature in time. Data taken from the beginning of December 2020 to the 20th of January 2021.

may not be exactly 32, and can vary over some average value.

The V2, V3 prototype pre-production versions of UUB should be more stable in this ratio and exhibit low variation. These versions of electronics were implemented in few stations in the array, to test their properties and behaviour during the real data-taking. For determination of the HG/LG ratio I chose the data taken in year 2020 by station 22 "Trak", because it did not have any outage in data taking during the year and should be very steady.

The method to compute the HG/LG ratio I used, was following. First, I computed the baseline of both channels as the average from the first 300 bins. Then, I subtracted the baseline B from both channels and summed the signal from high gain channel S_{HG} under the signal peak (from 660 to 700 bin). This sum was then divided by the signal from low gain channel S_{LG}:

$$R = \frac{\sum_{\mathrm{peak}}(S_{\mathrm{HG}} - B_{\mathrm{HG}})}{\sum_{\mathrm{peak}}(S_{\mathrm{LG}} - B_{\mathrm{LG}})}. \tag{5.3}$$

Very few events are suitable for computing the gain ratio in this way, as they have to fulfill a few criteria. Several cuts on data had to be applied. First I selected only those events, that were not saturated in any channel, because obviously the sum of the signal in that case would not be accurate. The next condition I required was that the signal in the low gain channel should pass the threshold of 40 FADC counts over the baseline for better recognition from the background noise. The last condition

was for the signal not to be long, so it will not leave few small peaks in trace but only one clear peak.

For events that survived these cuts, the HG/LG gain ratio was computed. The resulting histogram of these ratios is depicted in the picture Fig. 5.17. As we can see, the ratio has very low variation for all of the PMTs, which is always under 1.

The gain ratio for the SSD PMT could not be determined, as the number of suitable events for the calculation was not sufficient. This is mainly caused by triggering SSD by WCD.

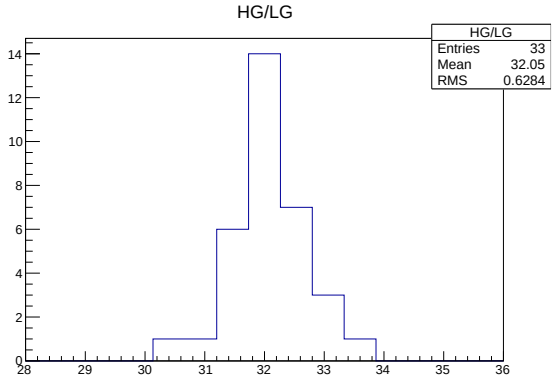

(a) PMT 1

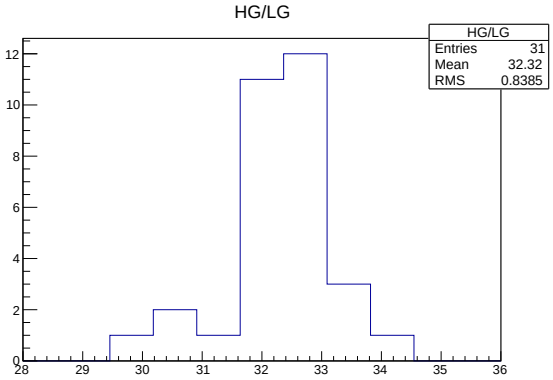

(b) PMT 2

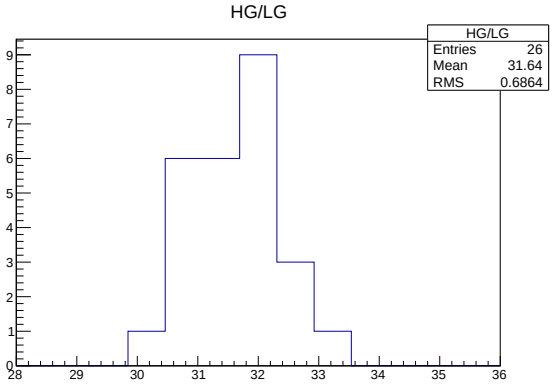

(c) PMT 3

Figure 5.17: Histograms for HG/LG ratio for three WCD PMTs of station 22 "Track".

Summary

This work was dedicated to the calibration of the surface detector of the Pierre Auger Observatory and also to the study of the properties of new electronics, that is a part of the AugerPrime upgrade.

The practical part of this work was focused on the calibration of the surface detector, particularly calibration histograms.

Calibration of the water Cherenkov detector is performed by the determination of the charge deposited by a vertically centered muon - VEM, which is obtained by the fit of the charge histogram formed by the measurement of background muons.
Calibration charge histograms were prepared for stations with old and new versions of electronics, that are already equipped with the scintillator detector. Next, the long-term evolution of the calibration quantities of the Water Cherenkovov Detector and the Scintillator detector was performed. It was confirmed, that the value of these quantities is influenced by the annual seasonal modulations. These temperature modulations are affecting the electronics of the detector, as well as the properties of water and the development of the shower in the atmosphere. Another chosen subject of research was the study of changes in the charge histograms after the addition of the scintillator. However, as the photomultipliers were recalibrated during the implementation of the scintillator, no direct effect of the added detector on histograms could be observed.

Next section was devoted to the study of a new approach for the surface detector calibration with the help of the scintillators. The motivation for changing the current detector calibration stems from the fact that due to aging effects, the muon peak cannot be resolved with a sufficient precision. Namely, the lowered reflectivity of the liner in stations leads to the increase in photon absorption. Requirement of a coincidence the scintillator events was proven to enhance the muon peak could help to improve the precision of the calibration.

The last part was devoted to the examination of the of the pre-production version of electronics of the surface detector, Upgraded Unified Boards (UUBs), that have already been installed in the array of the Observatory.
The output of the UUB is provided in two separated channels with different gains to enlarge the dynamic range. The first studied property of the V3 UUBs deployed in December 2020 was the behaviour of the baselines and the noises of the high gain channels with temperature. Data used for this analysis were recorded by the station 1729 from the beginning of December 2020 to the mid of January 2021. The computed values were the following. For the PMT 1, the average baseline value

$B = (244.4 \pm 0.6)$ ADC counts, and for the SSD PMT, $B = (231.9 \pm 0.9)$ ADC counts. The determined value of noise for SSD was $N = (1.96 \pm 0.14)$ ADC counts, and for the WCD PMT 1, $N = (1.97 \pm 0.15)$ ADC counts. Considering the large difference between the highest temperature during the day and the lowest during the night, which was approximately 21° C, the baselines were stable and the noises were low.
Next studied feature was the gain ratio of the high gain channel to the low gain channel. By design the ratios were expected to be 32 for PMTs in the Water Cherenkov detector and 128 for the Scintillator detector. The ratio was calculated to be (32.1 ± 0.6) for the PMT 1, (32.3 ± 0.8) for the PMT 2 and (31.6 ± 0.7) for the PMT 3. These results are satisfactory as the dispersion of the ratios for each PMT is not large. The gain ratio for the Scintillator Detector was not computed, as the number of suitable events for the calculation was not sufficient.

In the future, the temperature stability of the electronics modules will continue to be monitored and studied on all deployed stations. When the systematic effects are understood, it will become possible to analyze the shower data with the aim of disentangling the muonic and electromagnetic components.

Bibliography

[1] De Angelis, Alessandro, and Mário Pimenta. Introduction to particle and astroparticle physics: multimessenger astronomy and its particle physics foundations. Springer, 2018.

[2] Perkins, Donald H. Particle astrophysics. No. 10. Oxford University Press, 2009.

[3] Unger, Michael. "Cosmic rays above the knee." arXiv preprint arXiv:0812.2763 (2008).

[4] C. Amsleret al.[Particle Data Group], Phys. Lett. B667(2008) 1.

[5] The Pierre Auger Collaboration. "Combined fit of spectrum and composition data as measured by the Pierre Auger Observatory." arXiv preprint arXiv:1612.07155 (2016).

[6] Bustamante, M., et al. "High-energy cosmic-ray acceleration." (2010).

[7] Alves Batista, Rafael, et al. "Open questions in cosmic-ray research at ultrahigh energies." Frontiers in Astronomy and Space Sciences 6 (2019): 23.

[8] Longair, Malcolm S. High energy astrophysics. Cambridge university press, 2010.

[9] M. Ahlers, L. A. Anchordoqui, J. K. Becker, T. K. Gaisser, F. Halzen, D. Hooper, S. R. Klein. P.Mészáros, S. Razzaque, and S. Sarkar, FERMILAB-FN-0847-A, YITP-SB-10-01.

[10] Grupen, Claus, et al. Astroparticle physics. Vol. 50. Berlin: Springer, 2005.

[11] Zatsepin, Georgi T., and Vadem A. Kuz'min. "Upper limit of the spectrum of cosmic rays." JETPl 4 (1966): 78.

[12] Matthews, James. "A Heitler model of extensive air showers." Astroparticle Physics 22.5-6 (2005): 387-397.

[13] Aab,Alexander. "Air Shower Signal Shap e Analysis - ANew Metho d to Separate Ultra-High-Energy Photons from Cosmic Rays." Thesis. Radboud University Nijmegen. 2020.

[14] Haungs, A., et al. "Kcdc—the kascade cosmic-ray data centre." Journal of Physics: Conference Series. Vol. 632. No. 1. IOP Publishing, 2015.

[15] Pierre Auger Collaboration. "The Pierre Auger cosmic ray observatory." Nuclear Instruments and Methods in Physics Research Section A: Accelerators, Spectrometers, Detectors and Associated Equipment 798 (2015): 172-213.

[16] Xavier Bertou et al. Calibration of the surface array of the Pierre Auger Observa-tory.Nucl. Instrum. Meth., A568:839–846, 2006.

[17] Etchegoyen, A., et al. "Muon-track studies in a water Cherenkov detector." Nuclear Instruments and Methods in Physics Research Section A: Accelerators, Spectrometers, Detectors and Associated Equipment 545.3 (2005): 602-612.

[18] Aglietta, M., et al. Calibration of the surface array of the Pierre Auger Observatory. No. FERMILAB-CONF-05-281-E-TD. Fermi National Accelerator Lab.(FNAL), Batavia, IL (United States), 2005.

[19] Mockler, Daniela. "Reconstruction of Vertical Events Recorded by the Surface Detector of the Pierre Auger Observatory." 36th International Cosmic Ray Conference. Vol. 358. SISSA Medialab, 2019.

[20] Abraham, J., et al. "Trigger and aperture of the surface detector array of the Pierre Auger Observatory." Nuclear Instruments and Methods in Physics Research Section A: Accelerators, Spectrometers, Detectors and Associated Equipment 613.1 (2010): 29-39.

[21] Maris, Ioana Codrina. Measurement of the Ultra High Energy Cosmic Ray Flux using Data of the Pierre Auger Observatory. Diss. Forschungszentrum Karlsruhe, 2008.

[22] Aab, Alexander, et al. "Prototype muon detectors for the AMIGA component of the Pierre Auger Observatory." Journal of Instrumentation 11.02 (2016): P02012.

[23] Daniel, B., and Pierre Auger Collaboration. "The AMIGA enhancement of the Pierre Auger Observatory." Journal of Physics: Conference Series. Vol. 632. No. 1. IOP Publishing, 2015.

[24] Meurer, C., and N. Scharf. "HEAT-a low energy enhancement of the Pierre Auger Observatory." arXiv preprint arXiv:1106.1329 (2011).

[25] Schröder, Frank G., and Pierre Auger Collaboration. "Radio detection of high-energy cosmic rays with the Auger Engineering Radio Array." Nuclear Instruments and Methods in Physics Research Section A: Accelerators, Spectrometers, Detectors and Associated Equipment 824 (2016): 648-651.

[26] The cosmic ray energy spectrum measured using the Pierre Auger Observatory

[27] The Pierre Auger Colaboration. "Features of the Energy Spectrum of Cosmic Rays above 2.5×10^{18} eV Using the Pierre Auger Observatory." Physical review letters 125.12 (2020): 121106.

[28] Aab, Alexander, et al. "Muons in air showers at the Pierre Auger Observatory: Mean number in highly inclined events." Physical Review D 91.3 (2015): 032003.

[29] Bellido, Jose, and Pierre Auger Collaboration. "Depth of maximum of air-shower profiles at the Pierre Auger Observatory: Measurements above $10^{17.2}$ eV and Composition Implications." 35th International Cosmic Ray Conference. Vol. 301. SISSA Medialab, 2018.

[30] Aab, Alexander, et al. "Observation of a large-scale anisotropy in the arrival directions of cosmic rays above 8×10^{18} eV." Science 357.6357 (2017): 1266-1270.

[31] Abreu, Pedro, et al. "Measurement of the proton-air cross section at s= 57 TeV with the Pierre Auger Observatory." Physical review letters 109.6 (2012): 062002.

[32] Settimo, Mariangela. "An update on a search for ultra-high energy photons using the Pierre Auger Observatory." The Pierre Auger Observatory III: Other Astrophysi-cal Observations (2011): 17.

[33] Abreu, Pedro, et al. "Ultrahigh energy neutrinos at the Pierre Auger Observatory." Advances in High Energy Physics 2013 (2013).

[34] Pierre Auger Collaboration. "The pierre auger observatory upgrade-preliminary design report." arXiv preprint arXiv:1604.03637 (2016)

[35] Pierre Auger Collaboration. "Depth of maximum of air-shower profiles at the Pierre Auger Observatory. II. Composition implications." Physical Review D 90.12 (2014): 122006.

[36] Bretz, T., et al. "An integrated general purpose SiPM based optical module with a high dynamic range." Journal of instrumentation 13.06 (2018): P06001.

[37] A. Taboada. Analysis of the First Data of the AugerPrime Detector Upgrade. 2020. Doctoral thesis.

[38] Pierre Billoir. What is ageing in the tanks of the Surface Detector. 2014. GAP 2014 038.

[39] Koun Choi, Ioana C. Maris, Daniela Mockler. Long Term Evolution of the Area to Peak ratio. 2019. GAP 2019 028.